

The Inner Galaxy resolved at IJK using DENIS data

M. Unavane,¹ Gerard Gilmore,^{1,4} N. Epchtein,³ G. Simon,² D. Tiphène,³ B. de Batz,²

¹ *Institute of Astronomy, University of Cambridge, Madingley Road, Cambridge CB3 0HA, UK*

² *Observatoire de Paris-Meudon, DASGAL, CNRS/URA335, 5 place Jules Janssen, F-92195 Meudon Cedex, France*

³ *Observatoire de Paris-Meudon, DESPA, CNRS/URA264, 5 place Jules Janssen, F-92195 Meudon Cedex, France*

⁴ *Institut d'Astrophysique de Paris, 98bis Boulevard Arago, F-75014 Paris, France*

1 September 2021

ABSTRACT

We present the analysis of three colour optical/near-infrared images, in IJK, taken for the DENIS project. The region considered covers 17.4 deg^2 and lies within $|l| < 5^\circ$, $|b| < 1.5^\circ$. The adopted methods for deriving photometry and astrometry in these crowded images, together with an analysis of the deficiencies nevertheless remaining, are presented. The numbers of objects extracted in I, J and K are 748 000, 851 000 and 659 000 respectively, to magnitude limits of 17, 15 and 13. 80% completeness levels typically fall at magnitudes 16, 13 and 10 respectively, fainter by about 2 magnitudes than the usual DENIS limits due to the crowded nature of these fields. A simple model to describe the disk contribution to the number counts is constructed, and parameters for the dust layer derived. We find that a formal fit of parameters for the dust plane, from these data in limited directions, gives a scalelength and scaleheight of $3.4 \pm 1.0 \text{ kpc}$ and $40 \pm 5 \text{ pc}$ respectively, and a solar position $14.0 \pm 2.5 \text{ pc}$ below the plane. This latter value is likely to be affected by localised dust asymmetries. We convolve a detailed model of the systematic and random errors in the photometry with a simple model of the Galactic disk and dust distribution, to simulate expected colour-magnitude diagrams. These are in good agreement with the observed diagrams, allowing us to isolate those stars from the inner disk and bulge. After correcting for local dust-induced asymmetries, we find evidence for longitude-dependent asymmetries in the distant J and K sources, consistent with the general predictions of some Galactic bar models. We consider complementary L-band observations in a second paper.

Key words: Galaxy: stellar content – ISM: dust, extinction – Galaxy: structure – Stars: statistics – Stars: infrared – Galaxy : model – Galaxy : bar – extraterrestrial intelligence

1 INTRODUCTION

The central kiloparsec of the Galaxy is dominated by an extremely dense stellar cluster of unknown origin and history, and poorly known properties. It is unknown if this cluster is a remnant of the core about which the Galaxy grew, is the product of a later merger, is a product of a long-lived bar in the disk feeding gas into continuing star formation in the central galaxy, or has some other history.

Its relationship, if any, to the larger Galactic bulge, halo, and disk and to the smaller Galactic non-thermal nucleus is entirely unknown. This cluster, whose density approaches 10^6 solar masses per cubic pc, or 10^7 times that of the Solar neighbourhood, is the most extreme dynamical system available for detailed study.

The central degree or so is also an extended X-ray source, with temperature some 10^8 K , and gas pressures

1000 times those of the normal ISM. Moreover, the cluster changes its luminosity density profile by 2 in the power law index in some unobserved region between the central few arcsec and the optically observable region some degrees away. How and where? And are more complex spatial distributions possible? For example, in M31, the nearest similar spiral, the central region shows two luminosity maxima, neither of which corresponds to the centre of the larger scale gravitational potential, or is understood. (van der Marel et al. 1997)

In practice, because of the high extinction, it is necessary to work in the infrared.

Many high spatial resolution near IR wavelength studies of the central arcminute or so are available (cf Genzel, Hollenbach & Townes 1994) for a detailed review). However, remarkably little data is available concerning the larger scale structure. Balloon and satellite surveys (e.g.

COBE/DIRBE) are all of very low spatial resolution. The only large higher resolution survey, covering about $2^\circ \times 0.5^\circ$ around the galactic centre, is by Glass, Catchpole, and Whitelock (1987). It was performed in the J, H and K bands up to a limiting magnitude of $K=12$. While almost the entire J map was dominated by heavy interstellar extinction, those at H and K show progressively more detail of the inner region. They show clear changes in spatial structure for different populations, suggesting that analysis of low resolution data will necessarily be problematic

For the galactic centre this means that M and late K giants can be reached in K but not at the shorter wavelengths as the extinction will be too strong (up to 5 magnitudes in J [Catchpole, Whitelock & Glass 1990] leading to an expected apparent J magnitude of ≈ 16.5 mag; [Wainscoat et al. 1992]). We also expect that essentially all I and most J objects seen in the plane will be disk objects.

Two large scale, high resolution surveys in near infrared bands have begun recently. 2MASS (2-micron all sky survey) (Skrutskie et al. 1997) aims to survey the whole celestial sphere in J,H and K, with 2 arcsecond pixels, from two specially built identical telescopes in each hemisphere.

The second project is a European joint venture, called DENIS (Deep Near Infra Red Southern Sky Survey) which aims to map the whole of the southern sky in I,J and K with 3 arcsecond pixels. (Epchtein et al 1997). Technical details are given in Copet et al. (1997).

It is the data from this project which are relevant to the central regions of the galaxy that we consider in detail here, considering specifically the ability of DENIS-like survey data to study the inner Galaxy.

2 DENIS – DATA REDUCTION

2.1 Using the images

DENIS (DEep Near InfraRed Southern Sky Survey) (Epchtein 1997) will be a complete deep near infrared survey of the southern sky, with the objective to provide full coverage in 2 near infrared bands (J at $1.25\mu m$ and K at $2.2\mu m$) and one optical band (I at $0.8\mu m$), using a ground-based telescope and digital array detectors. Spare time at the end of DENIS observation nights during summer/autumn 1996 were used to take images in rasters (see Figure 2). Note that the shaded circle in this figure indicates the size of the DIRBE beam for comparison.

The standard pipeline processing of images ensures that for each image, sky subtraction is performed, the background is made flat, so that the images are ready for extraction of sources. (Borsenberger, 1997). The early pipeline extraction procedures proved unsatisfactory for these very crowded fields.

2.2 Source Extraction

Source extraction and aperture photometry were performed with the SExtractor software (Bertin & Arnouts 1996). Sources were extracted to 2σ above the background noise level, and an aperture of 3.5 arcseconds radius was used.

The calibration and flat fielding carried out in the preprocessing of the images is assumed to be sound. It is important to note that if a background map were to be constructed for each image as part of the source extraction procedure, it would remove one of the effects being studied (namely, the small scale variation of the extinction).

The most crowded fields have ~ 8000 sources in K, corresponding to a mean separation of ~ 10 arcsec, some 3 times larger than the radius of the aperture. The zero point was taken from standard star frames taken immediately before and after the observation of each raster.

2.3 Source matching between IJK

Each frame suffers its own distortions – software was developed to take triplets of corresponding I,J and K catalogues for a single image field, and map all onto a single consistent coordinate system. The chosen coordinate system, to make mapping straightforward, was chosen to be the coordinate system of the J frame. The choice is astrophysically motivated. The difference in the nature of the brightest sources in the presence of high extinction varies so much between I and K that matching these two would be unreliable if automated. The technique adopted uses the iterative fitting, with rejection of outliers, of a 2nd order, two-dimensional polynomial to several hundred of the brightest sources for the transformation between images. Higher-order transformations are found to be no better.

2.4 Absolute astrometry

The usefulness of these data cannot be fully realised unless cross matching with other databases is possible. To this end, *absolute* astrometry is required. After transformation of the positions of the I and K images to the J reference frame, we need to find a transformation between this J frame, and an absolute (α, δ) coordinate system. Examining available catalogues, we find that as of the time of writing, the catalogue with the greatest number of astrometric objects is the Hubble Guide Star Catalogue (GSC). This catalogue contains nearly 19 million objects, designed to satisfy the operational needs of the Hubble Space telescope. The objects are thus distributed almost evenly across the sky.

A DENIS image is about 12 arcminutes on a side, which means that, on average, the number of GSC sources found in an image is 18. However, the coverage is not entirely homogeneous. Near the Galactic plane, the regions of particular interest in this case, there are far fewer sources. For example, the $1^\circ \times 1^\circ$ around $\ell = 0^\circ, b = 0^\circ$ contains only 307 GSC sources, which corresponds, on average, to 12 per DENIS image. Poisson statistics tell us that there is then a 5% chance of ≤ 6 objects being found in an image. In fact, the patchiness of foreground extinction in these regions means that even Poisson statistics are an unreliable guide as to the number of objects we may find per frame.

Furthermore, at least second order fits are likely to be necessary to derive positions based on astrometric points, simply judging by the fact that a 2nd order transformation was needed between I and J images (taken by the same instrument, but using different optical paths, and detectors.) An average of 12 points per frame is not good enough to

fit the 12 coefficients required for such a fit – on average, the solution will be numerically unstable by being forced to provide 12 coefficients from just about 12 points, and about half the time (at least), there would not be enough points at all.

2.5 Digitised Sky Survey

The Digitised Sky Survey (DSS) is available on a set of CD-ROMS, and also online. In order to produce a list of astrometric points for use in performing absolute astrometry with DENIS, a viable option is to load relevant regions of the Digitised Sky Survey, source extract the images, and fit the GSC stars in that image to provide an astrometric database with a far greater density of objects.

For the region of interest indicated in fig 2, a grid of $1^\circ \times 1^\circ$ DSS images was overlaid to cover it. Each image was source extracted using SExtractor, the acceptance criterion being 2σ above background. The aperture ‘magnitudes’ obtained are unimportant, and do not relate linearly to the true magnitudes, since these images derive from photographic plates. However, they are useful in limiting the number of sources used for matching to the GSC, to a few hundred.

The GSC typically has 300 stars deg^{-2} in these regions. As in the case of the IJK images, the same software was used to make the transformations between (x, y) in the image and (α, δ) as determined by the GSC stars, projected to the local tangent plane.

The increase in density of astrometric reference points results in a density about 50 times greater than when using the GSC alone, leading to, on average, 500 points per DENIS image. We call this our auxiliary astrometric catalogue (AAC).

2.6 Using AAC

The I band images, taken at $\sim 0.8\mu\text{m}$, correspond closely in wavelength to the scans used for the DSS, and matching sources between them is a relatively straightforward exercise. Using the same technique as before, a 2nd order, two dimensional polynomial fit is made between the I images and the AAC extracted from the DSS. The catalogue of I images used is already transformed to J-image coordinates, so that the resulting transformation is directly from $J \rightarrow \text{AAC}$. Finally this $J \rightarrow \text{AAC}$ transform can be applied to all the image source coordinates to give 3 separate catalogues in I, J and K.

3 FINAL CATALOGUE

For each of the I, J and K bands, and for each raster as shown in figure 2, a final one-band catalogue is made, and sources duplicated in the overlaps of frames are removed. The overlapping images are used to give estimates of random astrometric and photometric scatter. (See later section on random errors)

For each raster, these large I, J and K catalogues are matched up. Seven classes of source are distinguished – those present in IJK, those present in JK only, those in IJ only, those in IK only (rare!), those only in I, those only in J and

those only in K. The matching is carried out by assigning initially as the same, objects closer than 3 arcseconds to one another in different bands.

The output catalogue contains Right Ascension and Declination for each of the 3 bands separately, a symbol indicating which of the 7 classes the object belongs to, and I and/or J and/or K magnitudes. The reason for keeping all 3 positions is explained in the following sections.

3.1 Astrometric and photometric precision of final catalogues

3.1.1 Random errors

The separations between matched objects in a complete raster (in this case C02), in each colour catalogue separately, is shown in figure 3.1.1. Some 70%, 80% and 75% respectively, in the I, J and K catalogues, have the same objects within 1 arcsecond of one another (no mean feat for 3 arcsecond pixels!). The random photometric scatter can be seen in the left of figure 3.1.1, again by comparison of duplicated sources from image overlaps. The figure indicates the difference between magnitudes m_1 and m_2 , measured from different images. A fit to the core values every $\frac{1}{2}$ magnitude gives values for the standard deviation of the difference $m_1 - m_2$, and since $\sigma^2(m_1 - m_2) = \sigma^2(m_1) + \sigma^2(m_2)$, m_1 and m_2 coming from the same underlying population, the standard random error in one measurement of the magnitude is given in each case by the $\sigma = \sigma(m_1 - m_2)/\sqrt{2}$. This distribution is indicated in the right panel of figure 3.1.1.

3.2 Systematic errors

The major systematic errors in magnitude measurement will be the result of crowding in the fields. The pixelsize used in the DENIS cameras is 3 arcseconds inevitably making it difficult to properly resolve sources in the crowded galactic centre regions.

We make an estimate of the size of this systematic photometric uncertainty by adding artificial stars to DENIS images. The images are then processed just as for the unaltered images, and the extracted magnitudes are compared to the input magnitudes.

These simulated sources are analogous to individual real sources – they can be considered as single additional sources in the presence of very many nearby sources. The statistics of the difference between the observed and generated magnitudes will be representative of the same statistics for real sources. (e.g. see Sodemann & Thomson 1997)

A crowded image (at roughly $\ell = 0^\circ$ and $b = 1^\circ$) was used as the base onto which artificial stars were added. Average values for the parameters of full-width at half-maximum, ellipticity, and orientation of the extracted sources in that image were found, and these were used to generate random sources. The sources were distributed at random over the image in steps of 1 magnitude from 11 to 17 in I, from 9 to 15 in J, and from 7 to 13 in K. Each image had 225 stars added (this is a small fraction when the number of sources per image is typically 4–5000). The resulting 7 images in

each band were treated as described above for the untreated images.

The derived catalogues were searched for the artificial stars to a distance of up to 3 pixels from their input positions. If found, their magnitudes and positions were noted. The magnitudes were characterised by a mean offset and a scatter about that mean offset.

The distribution of magnitude offsets is shown in figure 3.2. At the brightest magnitudes, there is little systematic shift in the magnitude due to the source extraction procedure. As higher magnitudes are reached, the measured magnitude (calculated using an aperture of 7 pixels diameter as indicated above) is systematically brighter than the actual magnitude. This can be understood in the context of the severe crowding as the result of the flux of nearby sources entering the aperture.

3.3 Completeness

Using the same simulations as above, the numbers of sources recovered within a given tolerance of the nominal position can be assessed and used as a measure of the completeness in these crowded fields. Figure 3.3 shows the fraction of simulated sources recovered from a typical crowded DENIS image, for various tolerances from the nominal position (1", 2" and 3").

Deviation (arcsec)	80% Completeness		
	I	J	K
1	15.8	12.6	9.9
2	17.0	13.6	11.3
3	>17	13.9	12.1

Note that these values are inferior to the expected limits for the DENIS survey in general, since we are confusion limited in very dense fields.

3.4 Multiband completeness

For ease of data treatment, the colour magnitude diagrams are made by considering only sources matched between pairs of images less than a fixed distance apart. In the next section, for the analyses, we use 1 arcsecond. This value has no meaning when considering the statistics only of I, J or K data, since we are not interested in the absolute precision with which the source position has been found, but only with the numbers of such sources at given magnitudes.

However, a tolerance of 1 arcsecond (or some other value) plays an important role in determining the distributions in IJ, JK and IJK statistics.

Presented below are the results of a Monte-Carlo technique for determining what fraction of IJ,JK and IJK matched images will be found if an upper limit is placed on their separation. The same artificial star experiments as above are used. We use the distribution of displacement from nominal position with magnitude (as indicated in a discrete manner in figure 3.3 for three values of displacement).

Taking the case of J and K as an example, we use the probability distribution for J and K for the displacement

from the nominal position and build up a 2-dimensional grid for the fraction retrieved according to the stringent criterion that the J and K sources lie within a given distance of one another.

Points are generated according to the measured probability distribution function, and the acceptance fraction is deduced using the numbers of J and K points which lie within 1 arcsecond of each other. The contour plot in figure 3.4 shows the result of this calculation, plotted on the same J–K,K plane as for the other plots. Shown in the figure are contours showing the probability of retrieval of a J–K pair, if the relative displacement tolerance is set at 1 arcsec. As expected, for objects bright in both bands (ie. low K and low colour), the retrieval probability is high, and this probability falls markedly as the K magnitude and/or colour is increased.

This diagram, smoothed by the fitting of a low-order two-dimensional polynomial is used below as a convolving mask applied to model colour magnitude diagrams to enable a quantitative comparison with the observed diagrams.

In exactly the same manner, an analogous analysis is carried out for the case of the I–J and J colour magnitude diagram. The same features are seen (bright blue objects are almost all retrieved, while dimmer, redder objects are not so well retrieved).

Finally, in the case of the two colour I–J and J–K diagram, contributions to a given part of the diagram come from objects of different magnitudes. At the brightest K magnitudes, as expected, the regions of low J–K value are essentially complete, and as we go to fainter K magnitudes, the completeness gets progressively lower. In a similar way, a three dimensional (K,I–J and J–K being the variables) polynomial is used as a mask.

3.5 Comments about completeness levels assigned

The test image used to derive these completeness results was an image at latitude $\sim 1^\circ$, where the source density in I,J and K is the highest of any position in the fields observed. In this sense, the completeness levels and estimates of photometric shifts are worst-case estimates. In general, completeness will be better, and photometric shifts less.

4 LOOKING FOR STRUCTURE

4.1 Overview

The data reduction described in the previous sections results in a wealth of point source data in the I,J and K bands. The region observed forms an irregular polygon contained within $|l| < 5^\circ$ and $|b| < 1.5^\circ$. The latitude coverage is greatest nearest to zero longitude, just as the longitude coverage is greatest near zero latitude. Figure 2 shows the coverage. The data is severely confused due to the large (3 arcsecond) pixels used coupled with the huge numbers of sources at low latitudes. The effects of crowding on photometry and completeness are described above.

In this section, we first present colour-magnitude diagrams for different parts of the region covered, and attempt to gain a qualitative understanding. Many of the unusual

morphological features in the CM diagrams can be understood in terms of crowding and completeness problems. The major effect seen in these diagrams is clearly that of a prominent, thin dust lane running through the fields centred near $b=0$.

A simple model is constructed to understand the colour magnitude diagrams resulting from observations of sources in a stellar disk in the presence of a strong dust layer.

With the aid of latitude-colour diagrams, we establish, using this model, parameters to describe the dust layer, and compare synthetic colour magnitude diagrams thus derived to the observed ones. It becomes clear that disk stars alone can describe many of the features in the appearance of the CM diagrams.

This model is then used to deduce the distribution in distance of the sources seen, in a statistical way, from the distribution in magnitude that results from the observations. Magnitude cuts are made in the luminosity functions corresponding to two regions, one dominated by near-disk objects, and the other by far-disk/bulge objects.

As a test of various Galactic bar models, the cuts above are used to remove the effect of nearby disk asymmetries, and to penetrate the far disk and central bulge regions. In J and K, asymmetries in the same sense as predicted by bar models are seen at the 3σ level.

4.2 Looking at the data

The dataset derived in the previous section is in three passbands (DENIS I, J and K centred at $0.8\mu\text{m}$, $1.25\mu\text{m}$ and $2.2\mu\text{m}$). The number of images processed is 613 in each passband, each covering an area of 770×770 arcseconds. The area covered is about 17.44 deg^2 , which means that double coverage occurs for 10.60 deg^2 (or about 60%). Excluding the poor quality data very near the edges, this becomes roughly 50% overlap. It is this which has allowed a good characterisation of random photometric uncertainties.

4.3 Numbers

The total number of sources extracted is some 1.500×10^6 in I, 1.707×10^6 in J, and 1.324×10^6 in K. After removal of duplicate observations the numbers become 0.748×10^6 in I, 0.851×10^6 in J, and 0.659×10^6 in K.

4.4 Colour-Magnitude and two-colour Diagrams

The following diagrams, (figures 4.4 – 4.4 and later), indicate, in the bottom left hand corner, a two-colour diagram with (J–K) on the abscissa and (I–J) on the ordinate. The top left panel in each case shows the colour magnitude diagram of J–K against K, with the (J–K) scale of the lower diagram being preserved. Finally, the bottom right panel shows the (I–J) against J colour-magnitude diagram rotated anticlockwise by 90° to match the (I–J) scale in the two-colour diagram. This is indicated diagrammatically in the explanatory figure 4.4. Note that each diagram is constructed separately, so that the number of points in the two-colour diagram will be fewest of all (requiring coincident I, J and K sources).

The first three sets of diagrams are for 0.2° latitude cuts between -0.1° and 0.1° , 0.4° and 0.5° and 1.0° and 1.2° (Figures 4.4, 4.4, 4.4). On each diagram is also marked a reddening line, calculated as in a later section.

Also shown, in figure 4.4, is a cut for a region around $\ell=3^\circ$ and $b=0^\circ$.

Before commenting on these diagrams, it is worthwhile to present colour-magnitude and colour-colour diagrams in the bands I, J and K for disk type III and type V objects. These will enable a comparison to be made. Figure 4.4 shows these diagrams. The data for the absolute K magnitudes are taken from a study by Garwood & Jones (1987), who produced a local disk luminosity function. The transformations to I and J are made according to data tabulated by Zombeck (1990). Notice that despite the wide range in absolute magnitudes, both the I–J and J–K colours have a very small intrinsic spread ($\lesssim 1$).

The magnitude cuts in I, J and K respectively are at magnitudes 11, 9 and 8 for the bright end (there are saturation problems brighter than this) and at 17, 15 and 13 at the faint end.

The most marked feature in figures 4.4, 4.4 and 4.4 is the straight line seen in the two-colour diagrams, which follows the reddening line. This demonstrates more clearly than anything else how important a role interstellar extinction plays in the interpretation of these diagrams. From figure 4.4, it is clear that intrinsic stellar properties will not contribute more than a magnitude of colour shift, so these diagrams immediately indicate that extinction in the line of sight of at least $A_V=10-15$ is to be expected. These figures also show some scatter to the right of the reddening line. This can be accounted for by crowding effects as will be demonstrated in a later section. Also, in the two-colour panel in figure 4.4, the highest latitude field, there is a clear bend at the reddest part of the line, so that objects are redder in (I–J), or equivalently, bluer in (J–K) than expected. Again, this is an effect which can be understood for this dataset in terms of crowding problems, and is discussed later.

The other panels in these figures are less easy to interpret. Some morphological features are clear. In the (J), (I–J) panels, there are clear striations running almost parallel to the reddening line. The very dominant blue faint part of the diagram, clear at the lowest latitudes, is much diminished at latitude $\sim 1^\circ$, while the fainter redder part becomes dominant. This can be plausibly understood in terms of a young, blue, main-sequence population whose presence will be stronger at the lowest latitudes in the disk. Features which are ‘reddened off the page’ become progressively more apparent at higher latitudes when the optical path through dust is lessened.

Similar features are evident in the (K), (J–K) diagrams, with the clear concentration centred at a colour of $J-K=4$ in figure 4.4 being shifted to $J-K\sim 3.5$ and $J-K\sim 2.2$ in figures 4.4 and 4.4 respectively. Again, this is plausibly due to a line of sight which sees less of the absorbing material in the disk.

Finally, figure 4.4 is included as an example of the inhomogeneous distribution of absorbing material in the line of sight. In all three panels, a clear break is seen in one

of the striations. In the (J),(I–J) panel, the striation starting at (J,I–J)=(13,3.6) and continuing to (11,2.0), shows a clear break in the direction of the reddening line, corresponding to a wall of extinction of $A_V \sim 3$. The same break is seen in the (K),(J–K) diagram in the striation starting at (J–K,K)=(2.0,12) and continuing to (1.2,10). This too is reproduced in the next sections by means of a model.

5 SIMPLE DISK MODEL

The approach we adopt in order to understand these colour-magnitude data is to construct a model of the Galactic disk from which we can generate sources, and make statistical comparisons to the observed data. Details of this model, and justification for its simplicity, are given in the appendix. Only a summary is given here. We employ a model which consists of a disk, exponential in both the vertical z -coordinate, and the radial coordinate. The dust is also represented as an exponential disk with its own scaleheight and radial scalelength.

For the stellar disk, we use recently derived values for the scalelength and scaleheight of 2.7 kpc and 0.20 kpc. (Freudenreich 1996, Kent, Dame & Fazio 1991) The small region of interest ($|l| < 5^\circ$, $|b| < 1.5^\circ$) is not very sensitive to changes in these disk parameters, but rather more to the dust layer parameters. The dust layer, and its appearance to us, is characterised by four parameters – the scaleheight of the dust (z_d), the radial scalelength (r_d), the height of the sun above the plane of this dust (z_0), and the strength of extinction in the midplane of the disk (A_V in mag/kpc). These are derived from a fit to the data.

The model output is convolved with the completeness levels and photometric scatter derived above and is subsequently compared to the observations. A sketch of the model geometry is given in figure 5

5.1 Luminosity Function

The brightest sources visible at near-IR wavelengths, as indicated in figure 4.4, are the later type giant stars.

5.1.1 Giants – Type III

As a source for a luminosity function for the type III (giant) stars, we refer to Garwood & Jones (1987), who observationally determined a local luminosity function in the K-band. Colours for local objects are taken from Zombeck (1990), who collates infra-red field star colours from a variety of sources. Colours for each of the types of source are given, from which a polynomial fit is made to determine an analytical transformation from the absolute magnitude in K, m_K , to the absolute magnitudes in I and J. (m_I and m_J). A second order polynomial was found to be sufficient in these cases, and the greatest discrepancy with the tabular values was less than 0.1 mag. The polynomials used are tabulated in table 5.1.

5.1.2 Main Sequence – Type V

Main sequence stars have intrinsically low near IR luminosities, mainly due to their small size. What some main sequence stars lack in size, they make up for in surface luminosity (i.e. high temperature) so that the brightest of these stars (O and B) despite having their peak in emission far from the near IR wavelengths we are interested in, nevertheless show bright magnitudes at these wavelengths.

We adopt the K-band luminosity function described by Garwood & Jones (1987). Again, we fit a low-order polynomial to fit the colours (J–K) and (I–K) as given by (Zombeck 1990). A third order polynomial is sufficient to prevent errors of greater than 0.1 mag. The polynomials are also shown in table 5.1.

It is assumed in this model that the luminosity function $\phi(m_K)$ and the geometrical parameters $\rho(x, y, z)$ are independent. This is an oversimplification since it is well known that the scale height of stars in the disk depends upon the stellar type (Schmidt 1963). Late type V stars (hence typically older) are to be found with large scaleheights while early type (and hence younger) stars have distributions with smaller scaleheights. The mechanism is clearly diffusive, as it is thought that stars form in the disk of the galaxy, and over the course of several revolutions diffuse to distributions with larger scaleheights. Giant stars, on the other hand, show an essentially constant scale height with type.

However, the majority of sources seen at the near IR wavelengths are the giant stars and the older type V stars, which can all be taken to have a (relatively) large scaleheight (some 2–300 pc).

As a test of this, below we show the luminosity functions at various heights above the plane, normalised to a scale height of 200 pc, generated by using the above luminosity functions, and scaleheight parameters for the different stellar types. The biggest differences occur between absolute magnitudes 0 and 3 (depending on waveband) where there are few sources that feature in the simulations presented. The three lines shown show the luminosity function at 3 different heights in the plane – $z=0$ pc, $z=200$ pc and $z=400$ pc (zero, one and two scaleheights of the oldest population).

We adopt a luminosity function for zero height (i.e. scale heights the same for the different stellar types) for the reasons given above.

5.2 Extinction coefficients for the DENIS filters

Since large values of extinctions along the line of sight play a major role in determining the appearance of the colour magnitude diagrams in the plane of the galaxy, it is important to establish precise values for the extinction coefficients. We use the tabulation by Mathis (1990) for the relative extinction in magnitudes as a function of wavelength. Between $1.25 \mu\text{m}$ and $3.4 \mu\text{m}$, we parametrise his tabulation as $\frac{A(\lambda)}{A(J)} = 1.484 - 5.60109x + 8.395624x^2 - 4.5947083x^3$ where $x = \log_{10}(\lambda/\mu\text{m})$. The error in this least-squares 3rd order fit is not more than 4%.

Referring to Copet et al. (1997), we use the instrument+sky response profiles in each of the I,J and K bands, and convolve them with the Mathis data to give the following values for $A(X)/A(1.25\mu\text{m})$:

Band (X)	$A(X)/A(1.25\mu\text{m})$	$A(X)/A(V)$
I	1.968	0.554
J	0.994	0.280
K	0.396	0.112

For comparison, the Mathis (1990) values of $A(\lambda)/A_V$ for wavelengths $0.90\mu\text{m}$, $1.25\mu\text{m}$ and $2.2\mu\text{m}$, corresponding to Johnson's I, J and K, are 0.479, 0.282 and 0.108.

5.2.1 Application to model

The chosen functional form for the dust layer is that of a disk exponential in both radial and vertical components. The amount of the dust is represented in terms of its absorption as:

$$X(r, z) = \propto e^{-z/z_d - r/r_d}$$

where X is a measurement of A_V in mag/kpc, and r and z are galactocentric cylindrical coordinates. The function is normalized by setting $dX/d\rho = X_0$, where ρ is distance along the line of sight and X_0 is the local extinction per unit distance. The functional form for the dust is integrated along the given line of sight to yield a function $A_V(\rho)$ which represents the amount of extinction in the line of sight up to a distance ρ from the sun.

5.3 Summary of model

In summary, the model consists of the following steps. Details of the Monte-Carlo method used to generate stars are given in an appendix.

(i) For given lines of sight, a probability distribution function of distance is generated. An extinction/distance curve is also generated by integrating the function representative of dust along the line of sight.

(ii) By combining functions in the three wavebands with the distance distribution, a limiting parameter w_0 is found to speed up the Monte Carlo process (see Appendix).

(iii) Observable distance/stellar class pairs are generated, and K magnitudes are calculated from the luminosity function.

(iv) Analytical representations in terms of the K magnitude are used to give the corresponding I and J magnitudes

(v) To each absolute magnitude, the modified distance modulus is added ($5\lg(r/\text{kpc}) + 10 + A_X$, where $X=I, J$ or K).

(vi) To each magnitude, is further added a random scatter in magnitude as determined by the artificial star experiments above.

(vii) A systematic magnitude offset to simulate crowding/extraction effects is added.

(viii) The source is rejected if its magnitude falls outside specified limits.

(ix) Steps 3–8 are repeated until the specified numbers of sources have been generated.

6 MODEL OUTPUT

Figures 6, 6 and 6 show the results obtained from running the model for three different latitudes $b=0^\circ$, $b=0.5^\circ$, and $b=1.1^\circ$, which may be compared with figures 4.4, 4.4 and

4.4 respectively. Figure 6 shows the result of a simulation where a cloud of extinguishing material with $A_V=3$ has been placed between 1.5 and 2.5 kpc from the sun in the line of sight. The raw output from the model has been treated with the systematic shifts and random scatter in photometry due to crowding, and the colour-magnitude and colour-colour diagrams have been convolved with the completeness masks derived at the end of the first section.

We stress again that these models are constructed for a disk only, and it is expected that whatever structure remains in the CM diagrams after the removal of this disk structure is attributable to the bulge. We show in figure 6 a quantitative comparison of the model for latitude $b = 0.5^\circ$ and the observations (figures 6 and 4.4). The figure shows the ratio of sources observed to those predicted in the model as a contour map over the (J–K)–(I–J), (J–K)–(K) and (I–J)–(J) planes. The dotted contours indicate small variations likely due to patchy extinction, for which account cannot be made in this model. The three dotted contours represent ratios of 0.5, 1.0 and 2.0. The solid contours represent number ratios from 4 up to 12. It is clear that in the (J)–(I–J) diagram, there is very little difference between the model and the observations. As expected for a diagram limited by the I band, distance penetration is low and only the disk is seen. However, for the (J–K)–(K) diagram, there is clearly an excess population of sources peaking at a colour of J–K \sim 3.5. This may be identified with a reddened giant branch in the bulge, which is in accord with the expectation that the power of the J and K bands to penetrate dust will allow the bulge to be seen. There remains a hint of this effect in the reddest sources of the two-colour diagram (J–K)–(I–J), but as for the (J)–(I–J) diagram, this is limited by the limited distance penetration of the I band, and will be well represented by a disk only. The ratio of bulge to disk sources seen here at $b = 0.5^\circ$ of $\lesssim 12$ is in good agreement with the result ($\lesssim 15$) we derive in a later section from published bulge/disk ratios.

The derivation of the parameters for the exponential dust-disk is detailed in the next section.

7 DERIVING THE DUST PARAMETERS

7.1 Elementary characterisation of dust layer

It is clear by looking even at integrated light images of the Galactic Central regions (e.g. Madsen et al., 1986) that there is a prominent dark band in the plane of the galaxy. This is due to the dust which pervades the disk, and causes light to be attenuated, especially at short wavelengths. The feature is diminished at longer wavelengths.

If we consider the dust to be a uniform plane of finite thickness $2d$, extending in the direction of the plane of the galaxy, with the sun centrally placed, we can easily calculate that the path length in the dust layer is given, in terms of the galactic latitude, b , by $d \csc b$. This optical path retains the same functional dependence on b if the uniform

layer is replaced by a dust distribution with an exponential dependence (For a vertical scaleheight of z_h , the result becomes just $z_h \csc b$).

Figure 7.1 shows the mean colours for cuts of height 0.2° covering the full range of the dataset from 5° to -5° . The colour shown is found by taking the mean value of all sources in the relevant colour-magnitude diagrams.

The variation with mean colour with latitude is mainly symptomatic, at these low latitudes, of extinction in the plane.

The major features in figure 7.1 are the clear rise in mean J–K colour towards the plane, and the equally clear fall in mean I–J colour towards the plane. These can both be understood in terms of different degrees of reddening and different populations sampled.

For the J–K diagram, the penetration into the dust is limited by the J waveband completeness. The dominant sources, seen to large distances, are type III giants, and the closer the approach to the plane, the greater the amount of dust in the line of sight, leading to a peaking in the mean colour towards the plane.

For the I–J diagram, the same effect will clearly be taking place, but the limitation in this figure is the effect of the dust convolved with completeness in the I waveband. Towards the plane, the distance observed is low, and the sources are dominated by nearby, main-sequence, blue stars. These have an intrinsic colour from $I-J = -0.2$ to 0.5 . As we look away from the plane, due to the decreased dust in the line of sight, we see to greater distances, and sample the giant stars visible to a much larger distance. The figure is effectively the same as the J–K figure (as suggested by the tails), with a large wedge removed from the middle due to the limited distance penetration at the wavelength of the I band.

It is also clear in the figure that there is an asymmetry about $b=0$ for the mean J–K colour of extracted sources. The peak, in fact, appears at $b \sim 0.15^\circ$. This can be attributed to a non-zero height for the sun above the plane of the local dust.

We can thus, using the I–J diagram, place a very approximate limit on the height of the extinction layer by noting that the abrupt change occurs at $\sim \pm 1^\circ$, and that the brightest main-sequence stars may be visible to distances of 2–3 kpc (Neckel & Klare 1980). One degree at this distance corresponds to about 40–50 pc, and can be seen as an indication of the scaleheight of the dust.

Similarly, a simple estimate of the displacement of the sun can be made by noting that in J and K bands, the typical colour of objects seen to any significant distance in the (dusty) plane is between 0.6 and 1.0 (type III objects – see figure 4.4).

Indicated on the left in figure 7.1 are *cosec* law fits of the tails of the distribution of extinction, using an intrinsic colour of $J-K=1.0$. The fits correspond to scaleheights differing by about 40%. i.e.

$$\frac{z_d - z_0}{z_d + z_0} = 1.4$$

where z_d is the scale height of the dust, and z_0 is the displacement of the sun above the plane. The solution we obtain is that $z_0/z_d \sim -0.17$. The fit is very insensitive to the intrinsic colour adopted. (e.g. changing $(J-K)_0$ from 1.0 to 0.6 changes z_0/z_d from -0.17 to -0.15).

Using the scale height of about 40–50 pc estimated above, we deduce that the sun lies about 7 pc below the local galactic dust plane.

And finally, noting that the reddest J–K colour of sources near $b=0$ is some 2.0–2.4 magnitudes redder than the intrinsic colour (corresponding to an A_V of 18–22), we can estimate, assuming DENIS sees some giants at the Galactic centre at about 8 kpc distance, that A_V is on average roughly 2.5 mag/kpc.

These estimates for the scale height, distance from plane, and A_V/kpc value can be refined in a model-dependent way.

8 MODEL DEPENDENT DERIVATION

The dust layer, in this simple model, is characterised by three parameters : the scaleheight of the assumed exponential profile (z_d), the radial scalelength (r_d) and the local rate of extinction (A_V in mag/kpc). In addition, the displacement of the sun from this midplane must be included (z_0).

The rough method described above provided initial estimates for the values of these three parameters – z_d, A_V in mag/kpc and z_0 . For the fourth parameter r_d , we use a value of 2.7 kpc as for the stellar disk, as a starting guess.

The model described above was set up with the adopted parameters for the stellar disk and dust scalelength, and the three parameters to be determined by a fit to the data (i.e. r_d, z_d, A_V in mag/kpc and z_0).

A $5 \times 5 \times 5 \times 5$ grid of synthetic colour-latitude diagrams was made by generating stars according to the model described above, using all the possible combinations of the following values of the three parameters:

- $r_d = 2, 4, 6, 8, 10$ kpc
- $z_d = 20, 30, 40, 50, 60$ pc
- $z_0 = -25, -20, -15, -10, -5$ pc
- $A_V = 0.5, 1.0, 1.5, 2.0, 2.5$ mag/kpc

The resulting point source data were convolved with the two-dimensional completeness functions derived in section 3 for the I–J and J–K data, and were subsequently used to generate colour-latitude diagrams by linear interpolation between points in this data tesseract. The statistic minimised is the sum of the squares of the difference between observed and model colours summed over both I–J and J–K colours. The ranges in latitude in each case were limited by practical factors.

In J–K, the ranges for comparison were limited to the tails of the distribution beyond $J-K=1$, so as to avoid the strongest bulge contamination. The tails of the J–K distribution are expected to sample to large distances, thereby averaging out, to some extent, local inhomogeneities in the dust distribution.

The same cannot be true for I–J - this will be severely affected by local inhomogeneities due to the limited distance sampled by the I waveband. Contrary to the situation in

the J–K figure, we expect the lowest latitudes to be little, if at all, contaminated by bulge sources, and a fit there is appropriate. We do, however, exclude the highest latitudes ($b > 1$) due to the known presence of very nearby (few 100 pc) dusty star forming complexes at positive latitudes which may severely bias the result (e.g. ρ Oph)

The 18 points thus chosen for the fit are the data points at latitudes $b = -1.2, -1.0, 1.0, 1.2, 1.4, 1.6, 1.8^\circ$ in J–K, and all points between -1.2° and 1.0° inclusive in I–J. All were given equal weight in a least squares fit. The statistic X used was simply the sum of squares of differences between the model and the observations:

i.e.

$$X = \sum_{i=1}^N (c_i - c(b_i; a_1, a_2 \dots a_M))^2$$

where c_i denote the observed mean colour values and $c(b_i; a_1, a_2 \dots a_M)$ denote the model derived mean colours. b_i is the latitude associated with that colour point, and $a_1 \dots a_M$ are the M parameters associated with the model. In the present case, $M=4$, and a_1, a_2, a_3 and a_4 are local A_V in mag/kpc, z_d, r_d and z_0 .

The number of data points, N , is 18 since the summation is over the limited set of 18 points in the I–J colours and the J–K colours from -1.2° to 1.8° inclusive in 0.2° steps.

This statistic can be used to estimate the standard deviation associated with each data point by means of the following formula (Press et al., 1992):

$$\sigma^2 = \frac{\sum_{i=1}^N (c_i - c(b_i; a_1, a_2 \dots a_M))^2}{N - M}$$

Minimising the statistic X with respect to variations in A_V, z_d, r_d and z_0 , we find a value $X=0.484$ occurring at values $A_V/\text{kpc} = 1.40$, $z_d = 40$ pc, $r_d = 3.4$ kpc and $z_0 = -14.0$ pc. An estimate for σ is thus 0.13, which agrees well with inspection of the plots. A value can thus be assigned to χ^2 by using the standard formulation:

$$\chi^2 = \sum_{i=1}^N \left(\frac{c_i - c(b_i; a_1, a_2 \dots a_M)}{\sigma} \right)^2$$

Subsequently, a 1σ estimate of the uncertainties in the parameters derived can be obtained by looking for the variations in those parameters which give rise to an increase in χ^2 of $\Delta\chi^2 = 1.00$ (Press et al., 1992). This corresponds to a value ΔX of 0.0346.

The result obtained in this way is:

- $A_V/\text{kpc} = 1.40 \pm 0.11$
- $r_d = 3.4 \pm 1.0$ kpc
- $z_d = 40 \pm 5$ pc
- $z_0 = -14.0 \pm 2.5$ pc

The model and observations are compared in figure 8. The fit to the wings of the J–K distribution is very good, which is as expected since the J–K sample is expected to sample a large path length of the disk, and any small scale inhomogeneities, such as the conspicuous +ve latitude nearby dust regions, are averaged out. The fit to the I–J data is less convincing as local structure in the interstellar dust strongly biases the mean colours.

Note that the above method does not use a truly independent value for σ . This is something which cannot be readily defined for the dataset. The uncertainties are not measurement error, but are due to the random nature of the extinction in the line of sight. As a consequence, the uncertainties in the results above reflect the uncertainties of this best fit within these limitations. They do not in any way indicate to what extent the functional forms are justified.

These dust distribution parameters are used in the model of the galaxy described above.

8.1 Comparison to other results

A whole sky fit to the COBE/DIRBE data has been made by Freudenreich (1996). He excluded the difficult central region ($\sim 40^\circ \times 30^\circ$) as well as other parts of the plane, and fitted a 28 parameter model, constraining simultaneously the scales and intensity of the dust layer, and the stellar disk.

Converting his dust layer parameters to the units used here, he gives:

- $A_V/\text{kpc} = 1.53 \pm 0.01$
- $r_d = 3.85 \pm 0.10$ kpc
- $z_d = 46 \pm 1$ pc
- $z_0 = 15.55 \pm 0.23$ pc

Freudenreich uses a functional form $\text{sech}^2(z/2z_d)$, as opposed to the form $\exp(-z/z_d)$ used here. These two forms are equivalent for $z \gg z_d$ (within a numerical factor of 4), but importantly, near $z = 0$ in the plane, these functions differ significantly. At height zero, they differ by a factor of 4, and at heights of z_d and $2z_d$, still by factors of 1.8 and 1.3. The fits made by Freudenreich exclude regions within a few degrees of the plane in most places, and he chooses the sech^2 functional form because it has some basis in theory as the density law of an isothermal self-gravitating disk (van der Kruit & Searle 1981). We find here roughly the same value of the parameter for scaleheight, but we assume an exponential form for the dust layer.

The values obtained for the intensity of local extinction, and the scale length of the dust layer are in good agreement. Integrating this model in a line of sight towards the centre results in a value for total A_V of 56. The wide uncertainty in r_d results in large uncertainties on this value between 40 and 110. Many observations towards the galactic centre (e.g. Becklin & Neugebauer 1968; Catchpole, Whitelock & Glass 1990) seem to agree on a value of extinction in the line of sight towards the very centre of the galaxy as $A_V \sim 40$, and our results are consistent with this.

The value we find for the distance of the sun from the local dust plane suggests that it lies below the plane of this dust (i.e. towards the South Galactic Pole). Indeed, looking at the surface photometry map produced using DIRBE data at $1.25\mu\text{m}$ (Weiland et al. 1994 – their figure 1), we see that the part of the bulge at negative latitudes appears brighter than that at positive latitude. Taken at face value, this would suggest a greater path length of dust towards the northern part of the bulge, and hence a position below the dust plane. However, as is clear from the same map after correction for extinction (Weiland et al. 1994), the most appropriate position for the sun is above the plane of the disk. This is further corroborated by many other studies using widely different methods. For example, Cohen (1995) finds

a distance of 15 pc above the plane by comparing north and south Galactic pole star counts. Figure 3b of Freudenreich et al. (1994) shows that the DIRBE $240\mu\text{m}$ emission lies below the Galactic plane, and though the relation between $240\mu\text{m}$ flux and dust is not well calibrated, this nevertheless suggests a displacement above the plane for the sun. Binney, Gerhard & Spergel* (1997) also find a value of 14 pc above the plane after modelling the inner Galaxy. Several more studies (e.g. Conti & Vacca 1990; Toller 1990) all agree on a value of $\sim 10\text{--}20$ pc above the plane. Clearly, all work to date is in agreement that the sun lies above both the Galactic stellar and dust planes.

Our result is not sensitive to the stellar plane, but rather to the dust plane – the stellar plane acts only as a luminosity source of near-constant colour. The simple model we construct imposes a global symmetry, and is fitted based on data from a very limited set of directions, unlike most of the other references cited above. We did not expect to derive globally reliable parameters which describe the three-dimensional complexity of dust distribution present in the disk/bulge, and indeed the position we derive for the sun is a demonstration of this fact. There is clearly asymmetry in the local extinction (for example, there is substantially greater extinction present north of the Galactic plane, much associated with the nearby ρ Oph star-forming region, than to the south). Presumably it is this which the analysis of the DENIS data is sensitive.

9 PECULIARITIES IN THE COLOUR-MAGNITUDE DIAGRAMS

Some of the peculiarities described above can be understood in a model dependent way.

9.1 Asymmetric Scatter to the right of the two colour line

Scatter can be seen to the right of the two-colour line as in figures 4.4,4.4,4.4. If real, these would represent objects with very high intrinsic J–K colour, compared to I–J colour. Figure 4.4 indicates that normal stars do not appear like this. It is possible that some of these are dust-enshrouded stars, which shine brightly at longer wavelengths, but are very much more obscured at shorter wavelengths. But before turning to these astrophysical explanations, we shall consider the data reduction.

Figure 9.1 shows the two-colour diagram for a typical crowded field, when the matching radius, within which all three images (I, J and K) must fall in order to be accepted, is varied between $0.3''$ and $3''$. It is clear that as the radius is decreased, spurious points scattered to the right of the line become fewer. If the matching radius for finding common sources between the 3 images is left too large (e.g. $3''$),

* Note that the preprint version (Binney, Gerhard & Spergel 1996) and the published version of the article by Binney, Gerhard & Spergel (1997) differ in the position ascribed to the sun. The preprint consistently states a position of 14 pc *below* the disk plane for the sun, while the published version states a value of 14 pc *above* the plane.

there are many sources apparently very far from the line. Reducing the matching radius to $1''$ loses some 10% of sources of deviation zero, but loses over 80% of those with deviation 2 magnitudes.

9.2 Bent two-colour line

In looking at the highest latitude colour-colour diagrams, (such as figure 4.4), we notice that I–J colours are too red compared with J–K colours at the same reddening. The two-colour line is effectively bent upwards.

AGB stars are expected to be found in this region of the colour-colour diagram. (Groenewegen, 1997) But another artifact of data processing can explain at least part of these bends, by attributing them systematic errors in photometry caused by crowded fields. The effect is well reproduced in the model when the systematic offsets in magnitude are included. Figure 6 shows a clear upward bend in the reddest parts of the two colour diagram. This can be understood in terms of the systematic effects in magnitudes. In particular, the J-band magnitudes show a very large offset for the faintest magnitudes retained, larger than those of the corresponding I and K magnitudes. The offset, for the reasons described above, causes the magnitudes to be too bright, or numerically, too low. This means that J–K is too low, and I–J is too high. This is precisely the effect seen in both the simulation and the observations.

9.3 Broken striations

Figure 4.4 shows a set of diagrams where striations in the colour-magnitude diagrams are fractured in the direction of the reddening line. This too is well understood in terms of the model by allowing a ‘wall’ of extinction in the line of sight, as demonstrated by figure 6.

10 DISTANCE DISTRIBUTIONS

The value of the simulated datasets, which are a good match to the observations, is that they can be interrogated for distance information, which will help to deduce the three dimensional distribution of stars in the inner galaxy. The information obtained in this way is summarised for the simulation at $b = 0.5^\circ$ in figure 10. This particular latitude has been chosen to enable the dust to be used to our advantage to separate source in the near disk and in the inner disk and bulge. At higher latitudes, the extinction due to dust is much less and penetration is good in all three bands. Near and far sources are not spread out by the reddening in the line of sight to a great extent. On the contrary, at very low latitudes approaching zero, the extinction is so severe that, given the magnitude limits of the system, it is not possible to see past the nearby disk population into the bulge regions, except possibly at K band.

From figure 10, it is clear that in the I band, due to the impenetrability of the local dust at short wavelengths, even the faintest magnitudes fail to penetrate very far from the sun. The situation changes at J band, where while penetration is low ($\lesssim 8$ kpc) at the lowest magnitudes (J=9.0–11.0), there is some penetration of the bulge regions at the

fainter magnitudes ($J=13.0-15.0$). At the K band, the penetration is even greater. Even the very brightest magnitudes may penetrate to the bulge region, but at the fainter magnitudes, the source counts are dominated by stars near the bulge. Remember that this simulation includes only a disk component, so when the model suggests penetration in as far as the bulge, the counts at that magnitude are likely to be dominated by bulge objects. This is shown in the contour plot above (figure 6), where the ratios of bulge to disk objects will be at $\lesssim 12$.

11 DISK/BULGE ASYMMETRIES

11.1 Bar models

There has been recent interest in the possibility of a kiloparsec scale bar at the centre of our galaxy. Various lines of evidence suggest the presence of a bar, and though they disagree on the exact parameters which best describe the form of the bar, they agree that the major axis is oriented towards the first quadrant. Methods employed include gas dynamics (Binney et al., 1991; Blitz & Spergel 1991), and modelling of integrated light distributions from the COBE/DIRBE experiment (Dwek et al., 1995; Binney et al., 1997). The asymmetries expected in projection are such that number counts at equally positive and negative longitudes should in general be greater at *positive* longitudes for large longitudes, and at *negative* longitudes at small longitudes.

Integration along the line of sight in such models for equal positive and negative longitude pairs results in different number counts for the two lines of sight. In figure 11.1, the number count asymmetries predicted by various models are shown. The effect of luminosity function will be small at these longitudes. The difference in distance modulus to the main concentration of the bar will be $\lesssim 1.0$ magnitude, since the separation in angle is at most 10° .

In practice, the amplitudes shown here will only be realised when a tracer population which samples only the bulge is used. In the present case, there is much disk contamination, and we expect, in general, a lower signal to be seen. An estimation of the extent of this dilution is given by integrating a recent model fit to the bulge/bar and the disk of the galaxy by Binney et al. (1997). For the purposes of this discussion, the contrast between disk and bulge in the inner disk is important. Using the model there, we find that for sources inward of 3 kpc from the centre, observed from the sun, and for longitudes of $\lesssim 5^\circ$, the number count contrasts vary strongly only with latitude (because of the thinness of the disk).

b(deg)	0.0	0.2	0.4	0.6	0.8	1.0
$f_{disk}/total$	0.12	0.08	0.06	0.05	0.04	0.03

These ratios are small, and in the light of other uncertainties present in this analysis, may be neglected.

In order to optimise detection of the inner-disk/bulge asymmetries in our data, we can use the information furnished by figure 10. We then test this for left-right asymmetries in the disk/bulge at various distances. We must first assume the similarity of disk luminosity functions at equal positive and negative longitudes for a give latitude of observation. This is not a contentious assertion, as the difference

in the lines of sight differs, in all the following cases, by less than 10° , so systematic age or metallicity differences are not expected.

The effect still remaining in the data which prevents immediate comparison between number counts at equal and opposite longitudes is caused by patchiness in the extinction, as there is no reason to expect this to be systematic. To minimise this effect, we use the model to identify magnitude ranges dominated by disk objects, and identify and correct for any associated (foreground) asymmetry.

That is, cuts in magnitude are chosen which are dominated by disk objects. A fit is made at these magnitudes between equal negative and positive longitude pairs. Any additional asymmetries remaining at fainter magnitudes will (in the case of the J band and K band) contain some signal of asymmetries in the inner disk or in the bulge. The I band, according to the model distances, should serve as a control, since it is not expected to penetrate very far, and the number counts seen should, after this correction for differences in extinction, show equal values at positive and negative longitudes.

12 RESULTS OF THIS EXPERIMENT

The magnitude limits chosen for the cuts are as follows:

Band	Fit region "Disk"	Test region "Bulge"
I	11.0–14.5	14.5–17.0
J	9.0–11.0	11.0–13.0
K	7.5–9.0	9.0–10.5

Figure 12 shows the results for $b = 0$ when cuts are made as described above to match the local disk luminosity function. The contrasts shown are for the fainter magnitudes as indicated above.

12.1 Deviation from unity

Do the contrasts deviate, in the mean, from unity? Taking the mean values of the contrasts in the three cases and finding the deviation of the mean we find the following:

Band	Mean, μ	σ_μ	$(\mu-1)/\sigma_\mu$
I	0.961	0.026	-1.5
J	1.105	0.037	2.8
K	1.118	0.039	3.1

The suggestion is that the I band deviates insignificantly (no more than 1.5σ) from unity. This is as expected, since the I band counts, though patchy, once matched for a pair of directions according to the local distribution of the brightest sources, show no further differences at faint magnitudes. The distance model above suggests that the penetration is not nearly deep enough into the disk to allow the innermost parts of the disk, or the bulge, to be sampled.

The J band shows a more significant deviation from unity in the ratio of counts ($\sim 2.8\sigma$). The distance model in this case suggests that penetration is deeper, and may

reach the inner disk and bulge. Indeed, the contrasts seen suggest that counts at negative longitudes are greater than those at corresponding positive longitudes. Similarly, in the case of the K-band number counts, we see a similar asymmetry. In this case, there is a marked dip in the contrast at a longitude of about 2 degrees. This is most plausibly due to a mixture of structural and extinction effects close to the centre of the galaxy. In the analysis here, we try to remove asymmetries in the nearby disk caused by dust to show up asymmetries in the inner disk or bulge. It is clear from the $^{12}\text{CO}(1J \rightarrow 0J)$ intensity plot shown in figure 12.1 (Dame et al. 1987) that there are distributions of material towards the centre of the Galaxy with intensities differing by several orders of magnitude over a very few degrees. In this light it is not surprising that the contrasts seen in the K number counts would not show any clear bar-like signature even if one existed. One approach to combatting this problem is to obtain multicolour information for sources in these regions and deredden each on a point by point basis. This technique is used in paper 2 to treat K and L band data.

The results here are at best inconclusive. The contrast seen in the K band is always, in the mean, greater than unity, suggesting that the asymmetric inner disk dust effects traced in figure 12.1 are a perturbation on a net greater negative longitude count compared with positive longitude counts.

A similar effect is not seen clearly in the J-band, which suggests that the realm of this central asymmetry, be it structural or due to dust, is not reached at this shorter wavelength.

13 CONCLUSIONS

We have derived some techniques to extract photometric and astrometric information from DENIS images in crowded fields and to characterise its deficiencies. We have used this dataset, covering a part of the region within $|l| < 5^\circ$, $|b| < 1^\circ$, to construct a model of the Galactic disk, and to fit parameters for a model of the dust layer. Using this model, we find that the large numbers of very red sources in the observed colour-magnitude diagrams, not reproduced by the model, can be understood as bulge giant branch stars. We assume the symmetry of the structure and luminosity function in the disk in directions of equal and opposite longitudes and fit number counts for a bright cut in magnitude (corresponding, according to the model, to near disk sources), and look for asymmetries in the fainter number counts (corresponding to inner disk and bulge objects). We find that in the I band, there is no asymmetry at fainter counts, consistent with the model-based expectation that the I band does not penetrate very far into the disk. In J and K bands, there is $\sim 3\sigma$ evidence for a ratio of negative longitude to positive longitude number count which is greater than one. This is consistent with the expectation from bar models.

This large scale statistical approach allows, to some extent, the possibility of ‘averaging out’ localised anomalies in extinction which are common in the plane, and towards the centre of the galaxy. However, as can be seen especially in the K-band contrasts, number counts can be seriously affected by the distribution of dust regions near the centre of the Galaxy itself. In the present set of observations, it is

not clear that the J-band data penetrates the densest dust regions reliably. One possibility is to use longer wavelengths where the extinction coefficient A_X/A_V is lower still, so that dust is a less severe problem. This method is explored in paper 2, where we combine DENIS K data and UKIRT nBL data ($3.6\mu\text{m}$, $A_{nbL} = 0.047 A_V$).

14 ACKNOWLEDGEMENTS

The DENIS project is supported by the *SCIENCE and the Human Capital and Mobility* plans of the European Commission under grants CT920791 and CT940627, the European Southern Observatory, in France by the *Institut National des Sciences de l’Univers*, the Education Ministry and the *Centre National de la Recherche Scientifique*, in Germany by the State of Baden–Württemberg, in Spain by the DGICYT, in Italy by the Consiglio Nazionale delle Ricerche, in Austria by the Science Fund (P8700-PHY, P10036-PHY) and Federal Ministry of Science, Transport and the Arts, in Brazil by the Fundation for the development of Scientific Research of the State of São Paulo (FAPESP).

MU would like to thank GS at the Observatoire de Paris for his hospitality during visits there, as well as Francine Tanguy, Jean Borsenberger and Lionel Provost for their help with access to the DENIS archive. MU acknowledges the financial support of the Particle Physics and Astronomy Research Council.

REFERENCES

- Becklin E.E., Neugebauer G., 1968, ApJ, 151, 145
 Bertin E., Arnouts S., 1996, A&AS, 117, 393
 Binney J., Gerhard O.E., Stark A.A., Bally J., Uchida K.I., 1991, MNRAS, 252, 210
 Binney J., Gerhard O., Spergel D., 1996, MNRAS, preprint astro-ph/9609066
 Borsenberger J., 1997, in *The Impact of Large Scale Near-IR surveys*, eds. F.Garzón et al., (Kluwer), p181
 Blitz L., Spergel D.N., 1991, ApJ, 379, 631
 Catchpole R.M., Whitelock P.A., Glass I.S., 1990, MNRAS, 247, 479
 Cohen M., 1995, ApJ, 444, 874
 Conti P.S., Vacca W.D., 1990, AJ, 100, 431
 Copet E. et al., 1997, A+AS, submitted
 Dame T.M., et al., 1987, ApJ, 322, 706
 de Jong R.S., 1996, A&AS, 118, 557
 Deul E., 1997, in preparation
 Dwek E. et al., 1995, ApJ, 445, 716
 Epchtein N., 1997, in *The Impact of Large Scale Near-IR surveys*, eds. F.Garzón et al., (Kluwer), p15
 Freudenreich H.T. et al., 1994, ApJ, 429, L69
 Freudenreich H.T., 1996, ApJ, 468, 663
 Garwood R., Jones T.J., 1987, PASP, 99, 453
 Genzel R., Hollenbach D., Townes C.H., 1994, RPP, 57,417
 Georgelin Y.M. & Georgelin Y.P., 1976, A&A, 49, 57
 Glass I.S., Catchpole R.M., Whitelock P.A., 1987, MNRAS, 227, 373
 Groenewegen M.A.T., 1997, in *The Impact of Large Scale Near-IR surveys*, eds. F.Garzón et al., (Kluwer), p165
 Hammersley P.L., Garzón F., Mahoney T., Calbet X., 1995, MNRAS, 273, 206
 Kent S.M., Dame T.M., Fazio G., 1991, ApJ, 378, 131
 Madsen C., ESO, Laustsen S., 1986, *ESO Messenger*, 46, 12

- Mathis J.S., 1990, ARA&A, 28, 37
 Neckel T., Klare G., 1980, A&AS, 42, 251
 Press W.H., Teukolsky S.A., Vetterling W.T., Flannery B.P., 1992, *Numerical Recipes*, (CUP)
 Schmidt M., 1963, ApJ, 137, 758
 Skrutskie M.F. et al., 1997, in *The Impact of Large Scale Near-IR surveys*, eds. F.Garzón et al., (Kluwer), p.25
 Sodemann M., Thomsen B., 1997, A+A preprint, astro-ph/9704282
 Toller G.N., 1990, in IAU Symp. 139, Galactic and Extragalactic Background Radiation, ed S.Bowyer & C. Leinart (Dordrecht: Kluwer),21
- van der Kruit P.C., Searle L., 1981, A&A, 95, 105
 van der Marel R.P., de Zeeuw P.T., Rix H.W., Quinlan G.D., 1997, Nature, 385, 610
 Wainscoat R.J., Cohen M., Volk K., Walker H.J., Schwartz D.E., 1992, ApJS, 83, 111
 Zombeck M.V., 1990, *Handbook of Space Astronomy and Astrophysics*, 2nd Edition, CUP
 Weiland et al., 1994, ApJL, 425, L81

15 APPENDIX – THE GALAXY MODEL CALCULATIONS

A Monte-Carlo method for generating stars in a Galactic model is mentioned above. Details of the method employed for optimising the Monte-Carlo process are given below.

For a given line of sight, a probability distribution is generated, $p(r)$, corresponding to the number of sources seen, per unit distance, due to the geometrical components included in the model. Clearly, because of the central concentration of the galaxy, this will mean that the peak in this distribution will lie at approximately r_0 from the sun towards the Galactic Centre (GC), where r_0 is the sun-GC distance.

Also for this line of sight, based on the dust model, a function $A_V(r)$ can be generated, which gives the extinction to any distance in that line of sight.

The luminosity function (LF) used has logarithmically more faint sources than bright sources.

Thus, if, independently, a random position is chosen according to $p(r)$ and a random stellar type is chosen according to the LF, the resulting pair will most likely be a faint, main sequence star near the Galactic Centre – which will not be visible.

The Monte Carlo approach used to generate random points in this two dimensional space of distance and luminosity function will in general be very wasteful. We derive a method for limiting the space in which random points are thrown, and which also ensures that the very low probability near and faint objects are accurately included in the number counts.

The functions embodied in the model generate, for a given line of sight, the PDF (the probability per unit distance that a point will be found there) and $A_V(r)$ curves (integrated flux diminution up to that distance). Examples are shown for a line of sight in the direction $\ell = 4.0^\circ$ and $b = 0.2^\circ$ in figure 15.

15.1 Distance

First of all, the function $p(r)$ is converted to a function of distance modulus, D_m . Noting that

$$p(r)dr = p(D_m)dD_m$$

and that

$$D_m = 5 \lg(r/kpc) + 10$$

we obtain

$$p(D_m) = \frac{dr}{dD_m} p(r) \propto r p(r)$$

This function is then numerically integrated to give a function

$$F(D_m) = \frac{\int_{-\infty}^{D_m} p(D'_m) dD'_m}{Q}$$

where the normalisation Q is given, in terms of the upper limit D_m^0 in D_m chosen for the simulation, by:

$$Q = \int_{-\infty}^{D_m^0} p(D'_m) dD'_m$$

Figure 15.1 shows both $p(D_m)$ and $F(D_m)$ for the example shown in figure 15.

This function $F(D_m)$ is subsequently numerically inverted, so that the input of a random deviate uniformly distributed between 0 and 1 will result in an output D_m distributed according to the PDF for the line of sight.

Figure 15.1 shows the result of this inversion, with the ordinate $\ln x$, where x is a uniformly distributed deviate between 0 and 1. Furthermore, corresponding to each distance modulus, D_m , we can assign a value A_V from the lookup diagram shown in the upper panel of figure 15. Each waveband, I, J and K, corresponds to a different value of extinction, A_I, A_J, A_K . These three modified distance modulus curves are shown in the figure.

15.2 Luminosity Function

The luminosity functions may be treated in a similar way to the distance modulus distribution. Taking the K-band luminosity function as an example, we can, as before, generate a cumulative distribution, invert it, and use this as a lookup table to convert a deviate, y , uniformly distributed between 0 and 1 into a corresponding stellar type.

15.3 Combination

To limit the numbers of sources which are tried only to those brighter than some given magnitude limit, let us denote by x and y two independent uniform random deviates between 0 and 1. From x , we derive a modified distance modulus according to the distance modulus and reddening combined lookup table, as in figure 15.1. From y , we deduce a stellar type in the same way. The overwhelming likelihood is that a faint source at large distance is generated, which will clearly fall out of the magnitude range of interest.

In figure 15.3, there are a multitude of lines. Concentrating on the long-dashed line, we see that combining the x figure for modified distance modulus for K-band, and the y figure for K-band luminosity function, limits in observed K magnitude are expressed by lines roughly parallel to lines of constant $w = \ln x + \ln y$, or constant xy . Similarly, magnitude limits can be set for J and I, leading to the limiting lines shown (dotted and dashed lines).

15.4 Generation

The aim is to take two independent uniform deviates between 0 and 1, u and v , and convert them to deviates x and y which uniformly cover the space ($x = 0 \rightarrow 1, y = 0 \rightarrow 1$) excluding the region with $w < w_0$.

Graphically, we seek to fill only the left region in figure 15.4, where the bounding function is $xy = e^{w_0}$.

Now for uniform deviates x and y , the product $z = xy$ will be distributed as

$$p(z)dz = \int_z^1 dx \int_{\frac{z}{x}}^1 dy - \int_{z+dz}^1 dx \int_{\frac{z+dz}{x}}^1 dy$$

or

$$p(z) = -\ln z$$

To well sample the lowest probabilities, we convert this to a function in terms of $w = \ln z$, to give $p(w) \propto -we^w$. We then integrate and normalize this function to find a cumulative form, with a lower limit w_0 and upper limit w_1 ($w_0, w_1 \leq 0$). The result is:

$$F(w) = \frac{e^{w_0}(1-w_0) - e^w(1-w)}{e^{w_0}(1-w_0) - e^{w_1}(1-w_1)}$$

As before, when this is inverted, a uniform deviate, u between 0 and 1 can be supplied, and the value w corresponding to $F(w) = u$ gives a value for $w = \ln x + \ln y$ such that the points (x, y) are uniformly distributed in the allowed region.

By symmetry, x and y are distributed in the same way for any given value of xy . We can thus find values x and y by using the second uniform deviate v . Constructing $d = w(2v - 1)$, we obtain a uniform deviate between $-w$ and w . This corresponds to the difference $\ln x - \ln y$. This leads to the final result, that if a deviate w and a secondary deviate d are generated as described above, then

$$\ln x = \frac{d+w}{2}$$

and

$$\ln y = \frac{d-w}{2}$$

where points (x, y) are uniformly distributed in the allowed region.

The amount of the $x - y$ plane excluded by limiting sources to the left of the line $xy = z_0$ is given by $z_0(1 - \ln z_0)$, or $e^{w_0}(1 - w_0)$ where $w_0 = \ln z_0$.

In the example illustrated, a limit of $w_0 = -10$ allows all observable sources to be generated. This corresponds to sampling only 1/2000th of the xy plane. In general, we find

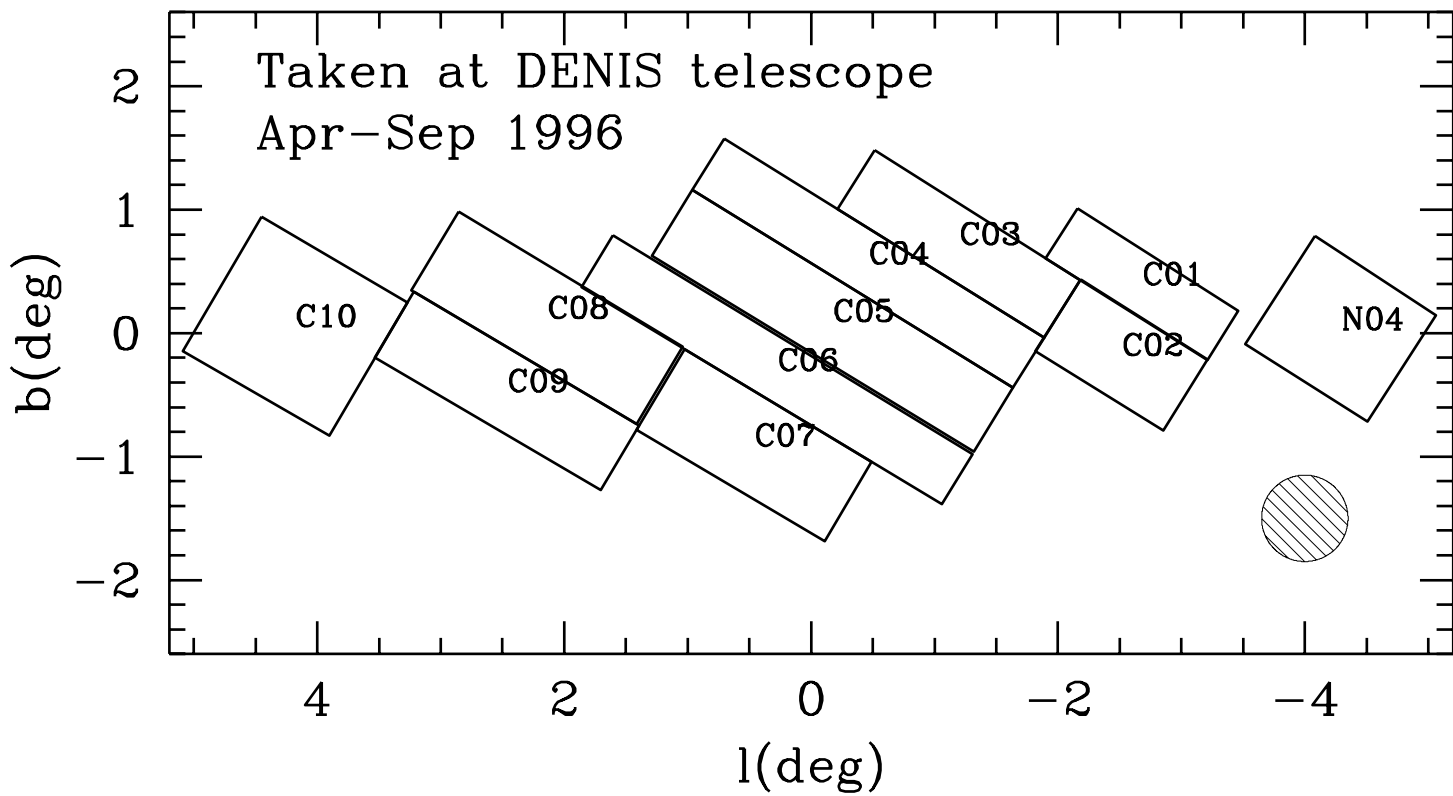
that w_0 lies between -7 and -10 , allowing savings in processor time by a factor of between 140 and 2000. The algorithm described was translated into the Super Mongo (SM) programming language before use.

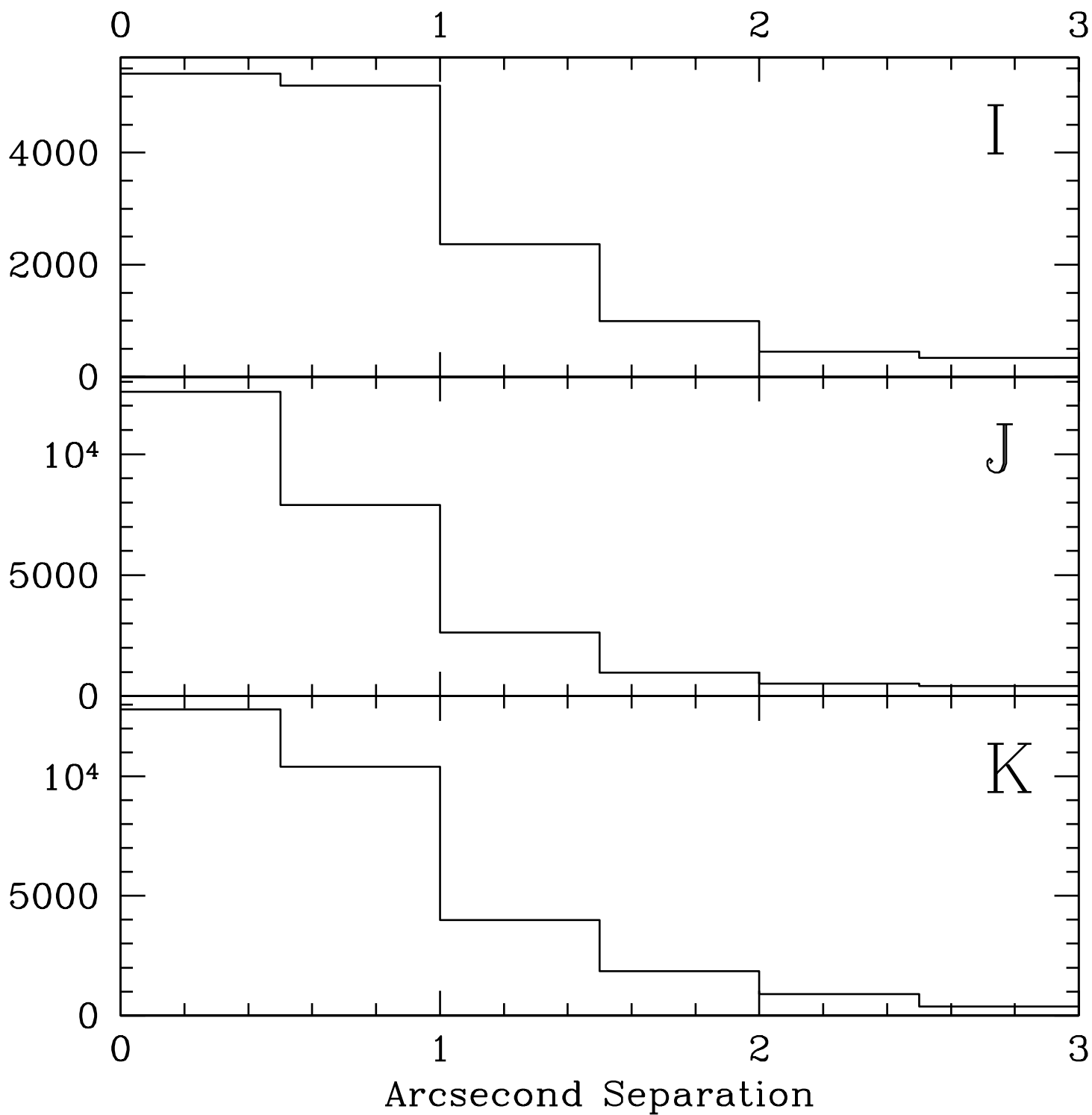
15.5 Comments about Spiral Arms

It is not clear what the contrast between arm and interarm regions is likely to be at near IR wavelengths. The dominant emission is from giant stars, which will plausibly have diffused away from the sites of young star formation associated with spiral arms. Furthermore, dust associated with the spiral arms, which plays a role in increasing the contrast at short wavelengths, has a lesser effect at longer wavelengths. Hence the contrast is likely to be less beyond $1\mu\text{m}$ than below it. Studies of external disk galaxies (de Jong, 1996) suggest that the contrast may be $\lesssim 3$, which is in agreement with recent DIRBE based model-dependent analysis of our galaxy (Binney, Gerhard & Spergel 1996). It is not even certain that well-defined spiral arms are observable at all wavelengths. Independent observations using bright O stars to probe the disk (Neckel & Klare 1980) and HI regions (Georgelin & Georgelin 1976) yield different spiral arm structure.

However, the limited directions to which the model is to be applied in this case – the inner 10° of the galaxy – means that lines of sight will in general pass perpendicularly to the directions of any spiral arms which may be in the disk. For the purposes of investigating longitude dependent asymmetries, lines of sight perpendicular to the arms and separated by no more than 10° will not have a very different amount of spiral arm signature present.

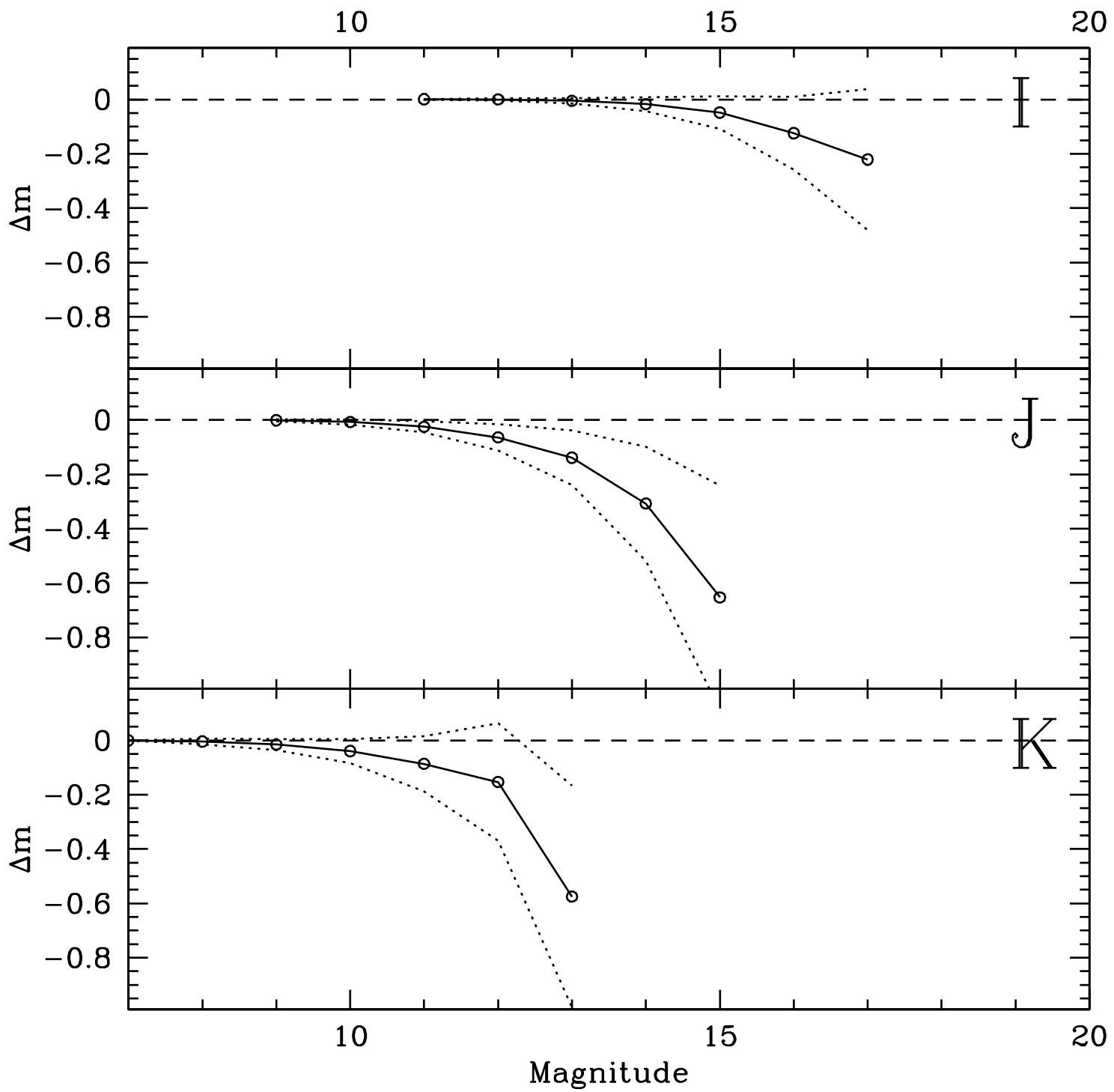
For these reasons, and anticipating the method used to remove near disk signature from number counts, we do not include spiral structure in the model. For reference, a sample set of colour-magnitude diagrams is shown when spiral arms are included. Spiral arms of gaussian width 0.5 kpc are placed in the line of sight at distances 3.4, 5.1 and 6.9 kpc from the Galactic centre in accordance with the model of Georgelin & Georgelin (1976), and are given an enhancement of a factor of 3 with respect to the underlying disk density. (figure 15.5). No modification is made to the dust model. There is only a slight hint of difference between this model and the comparison model without spiral arms (figure 6), and it is not useful at this level, to include this subtlety in our model.

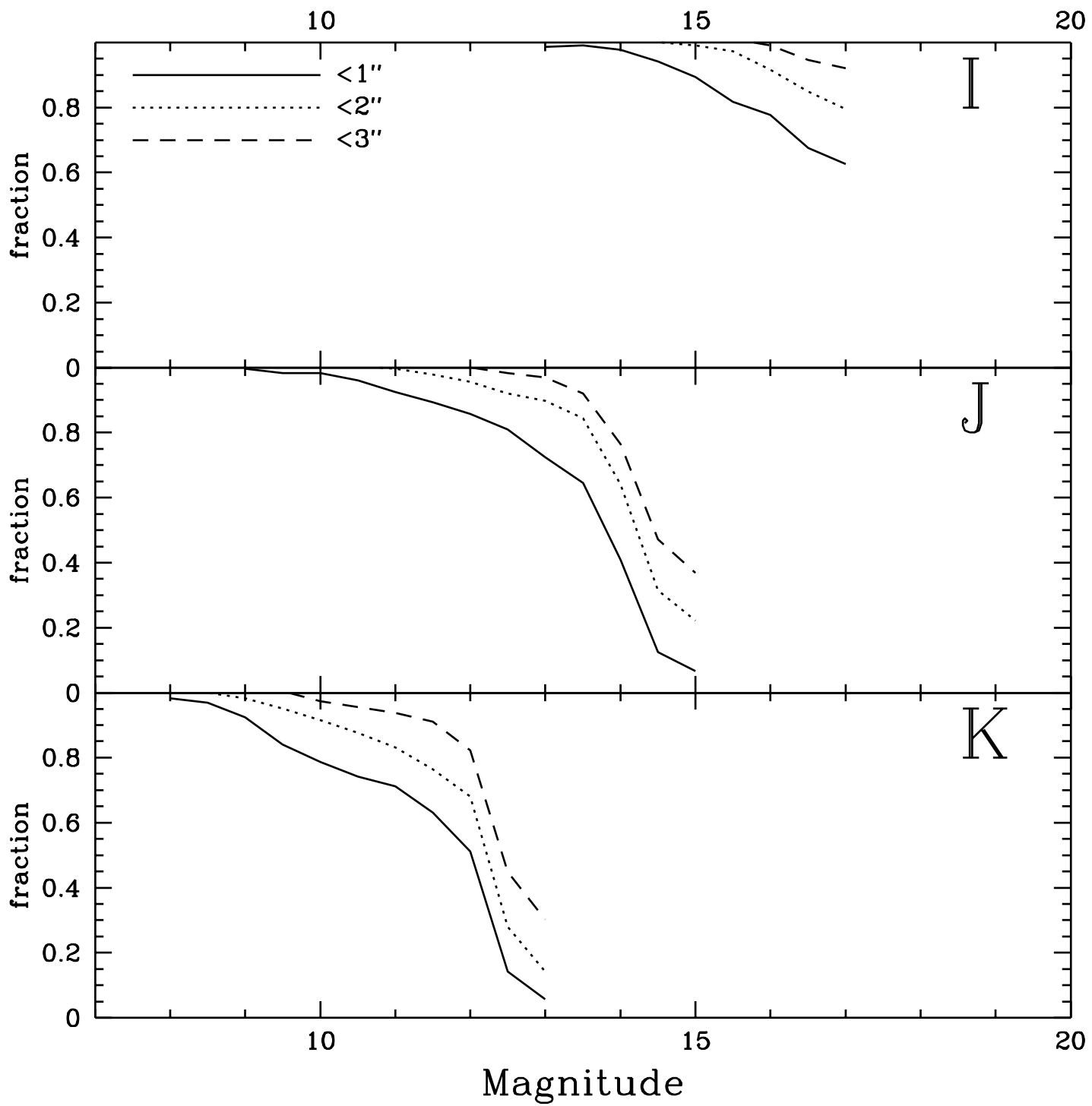


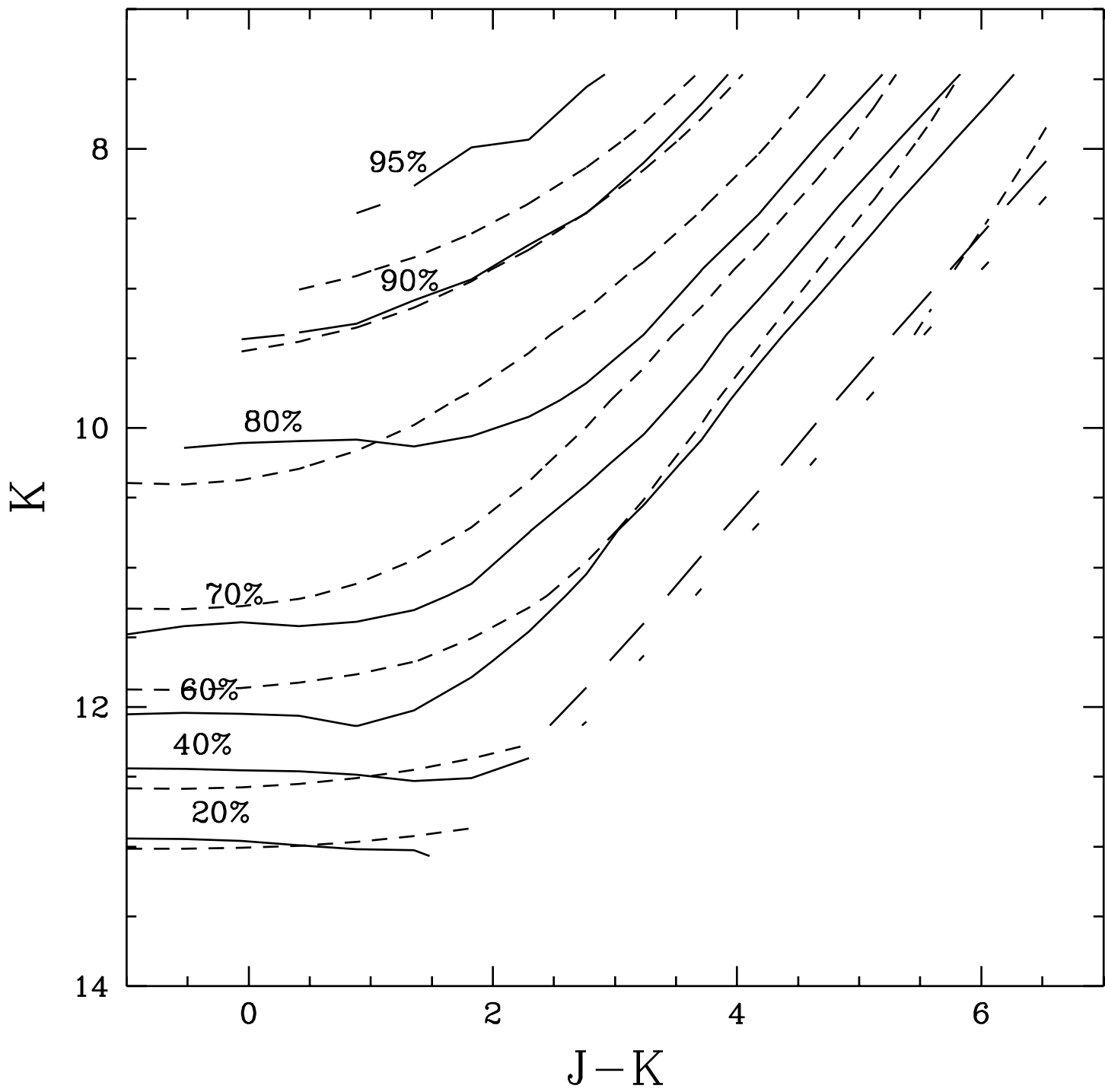


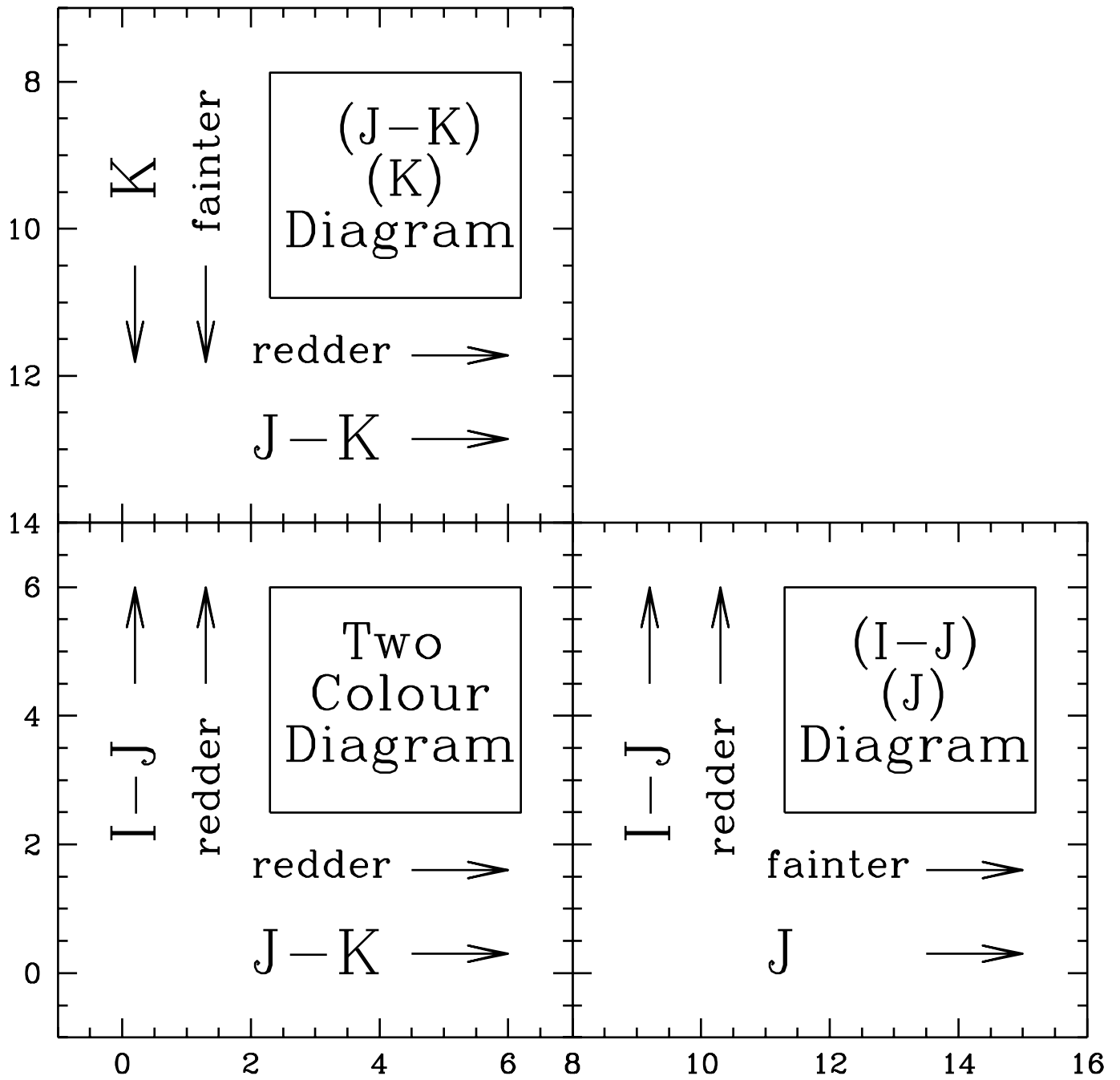
This figure "figure3.gif" is available in "gif" format from:

<http://arxiv.org/ps/astro-ph/9710317v1>









This figure "figure8.gif" is available in "gif" format from:

<http://arxiv.org/ps/astro-ph/9710317v1>

This figure "figure9.gif" is available in "gif" format from:

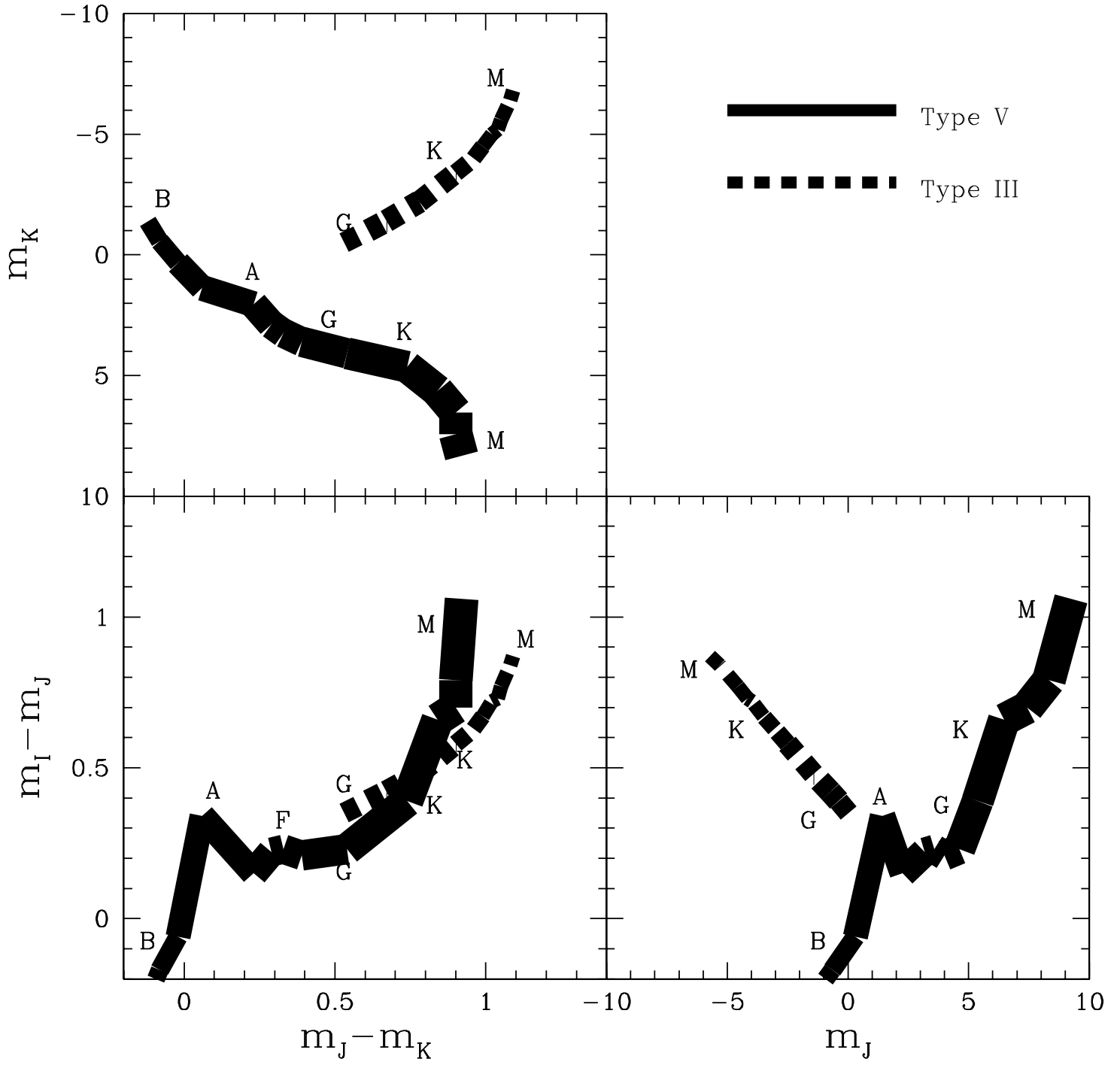
<http://arxiv.org/ps/astro-ph/9710317v1>

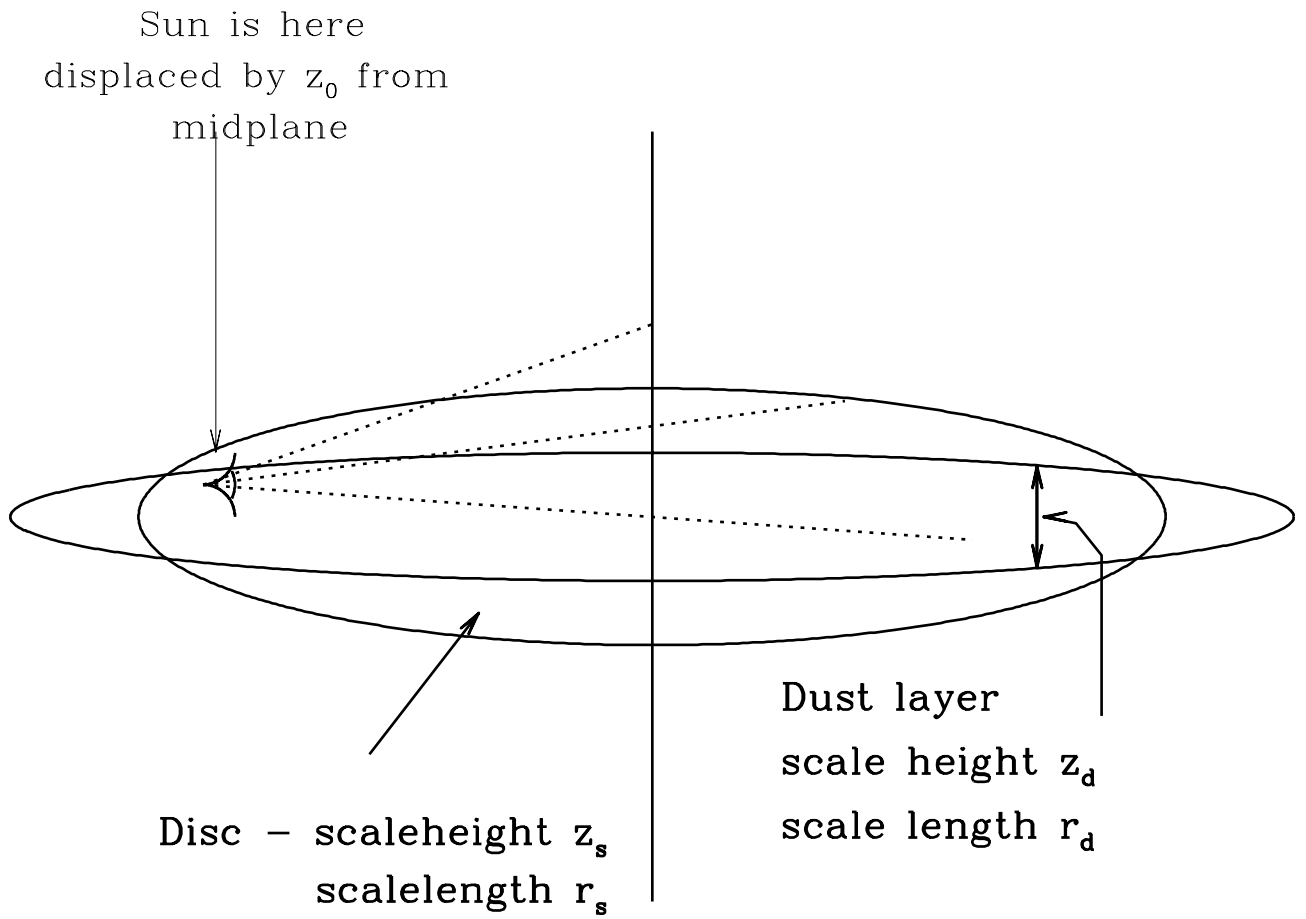
This figure "figure10.gif" is available in "gif" format from:

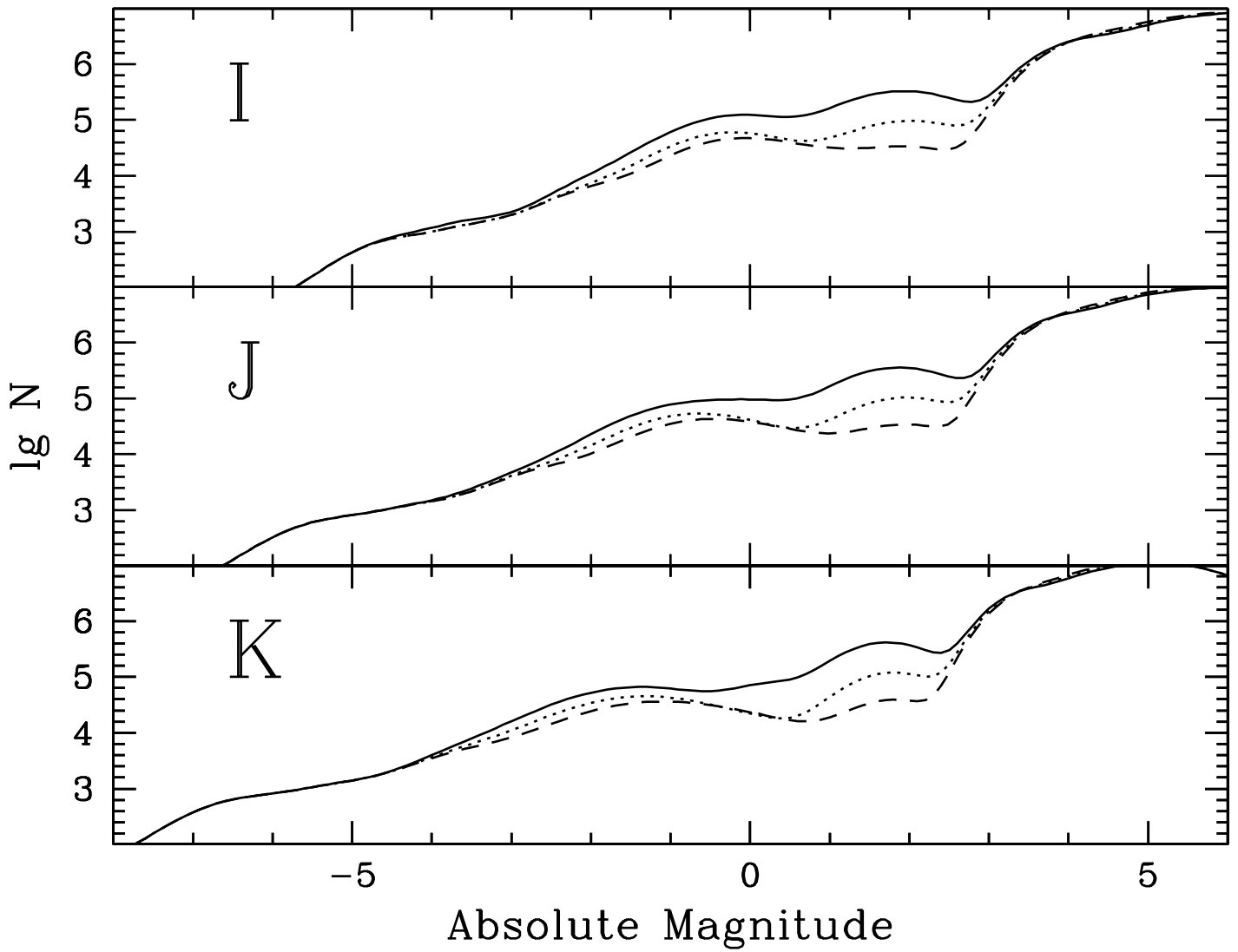
<http://arxiv.org/ps/astro-ph/9710317v1>

This figure "figure11.gif" is available in "gif" format from:

<http://arxiv.org/ps/astro-ph/9710317v1>







This figure "figure15.gif" is available in "gif" format from:

<http://arxiv.org/ps/astro-ph/9710317v1>

This figure "figure16.gif" is available in "gif" format from:

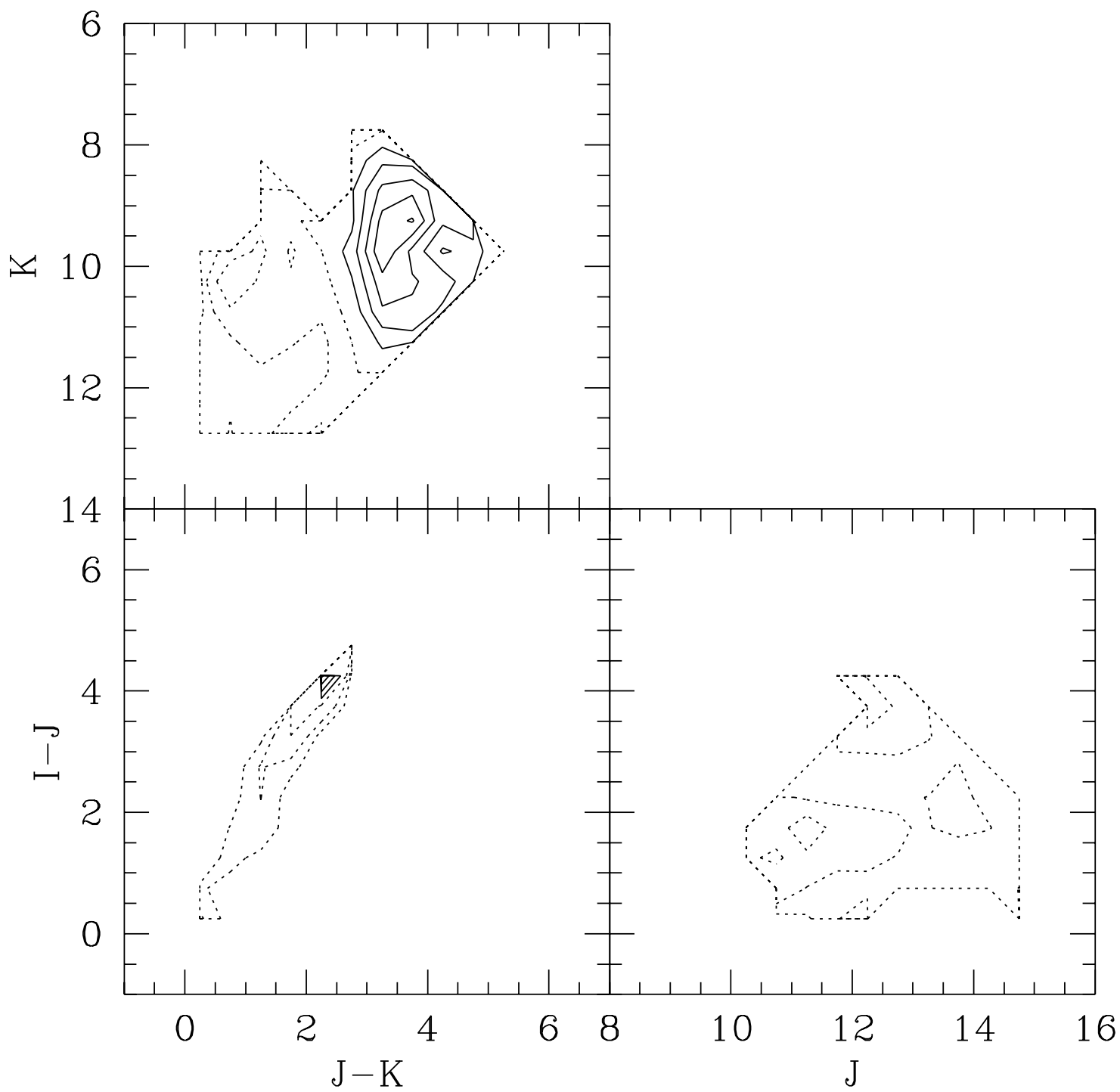
<http://arxiv.org/ps/astro-ph/9710317v1>

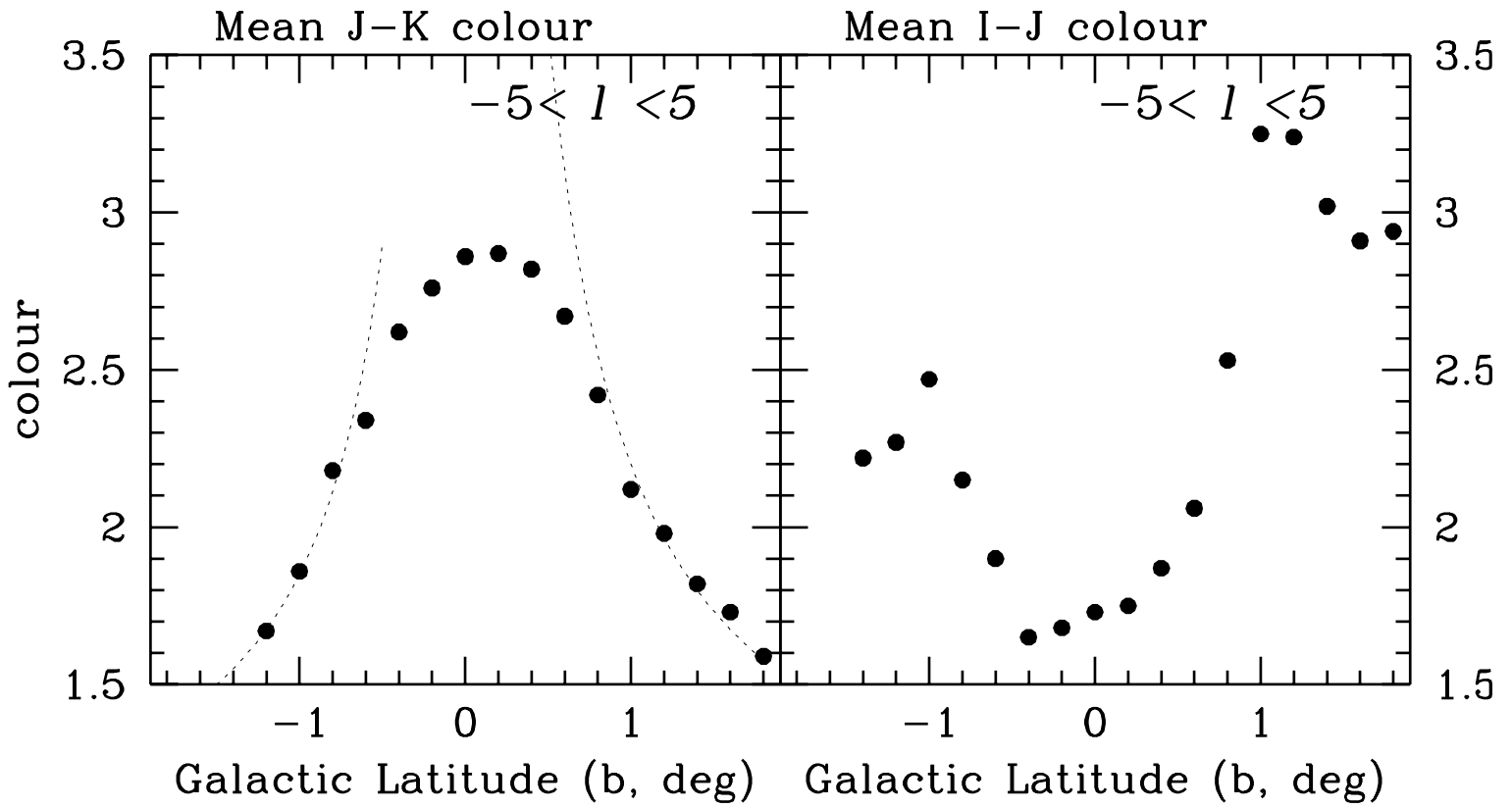
This figure "figure17.gif" is available in "gif" format from:

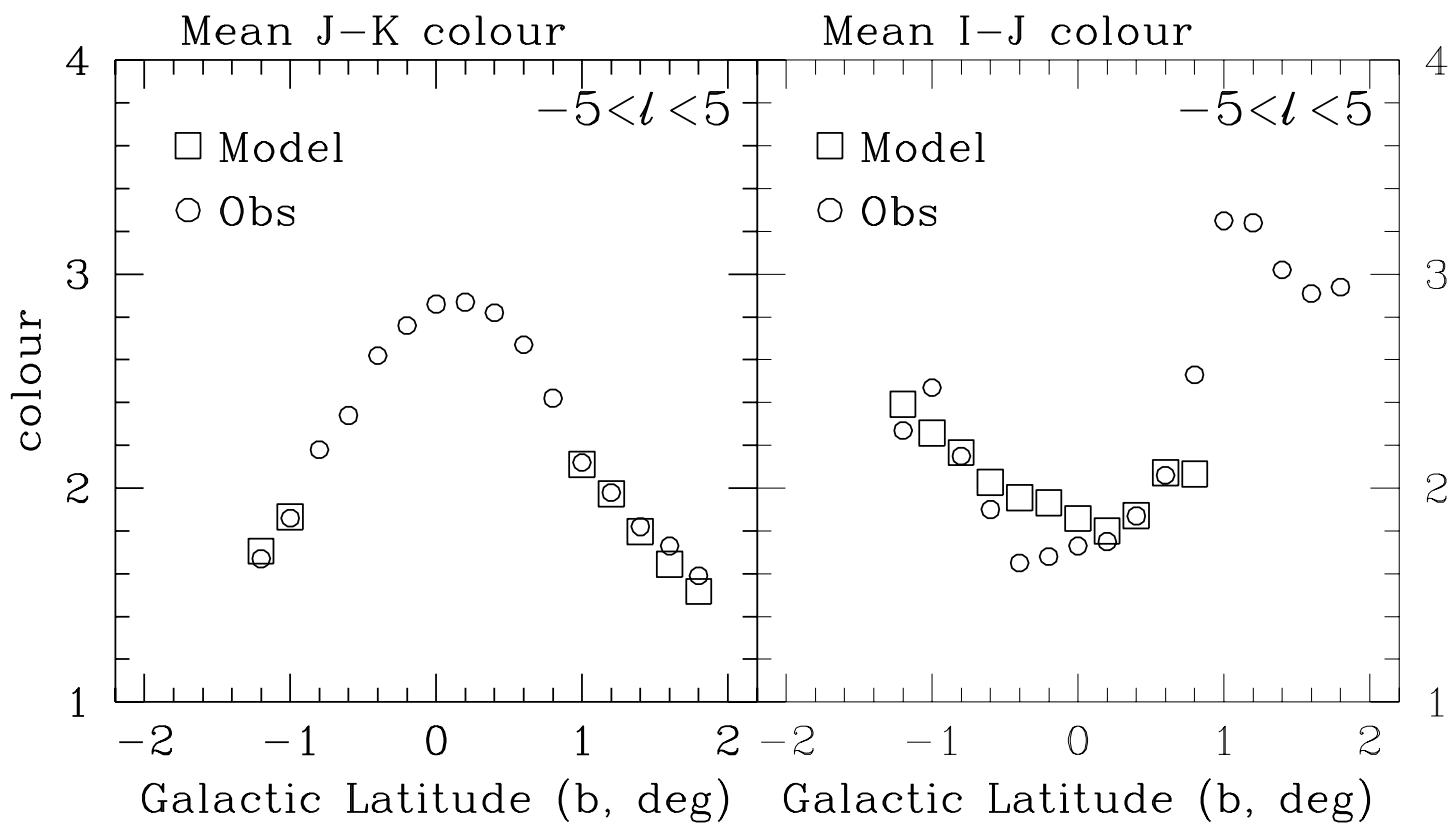
<http://arxiv.org/ps/astro-ph/9710317v1>

This figure "figure18.gif" is available in "gif" format from:

<http://arxiv.org/ps/astro-ph/9710317v1>





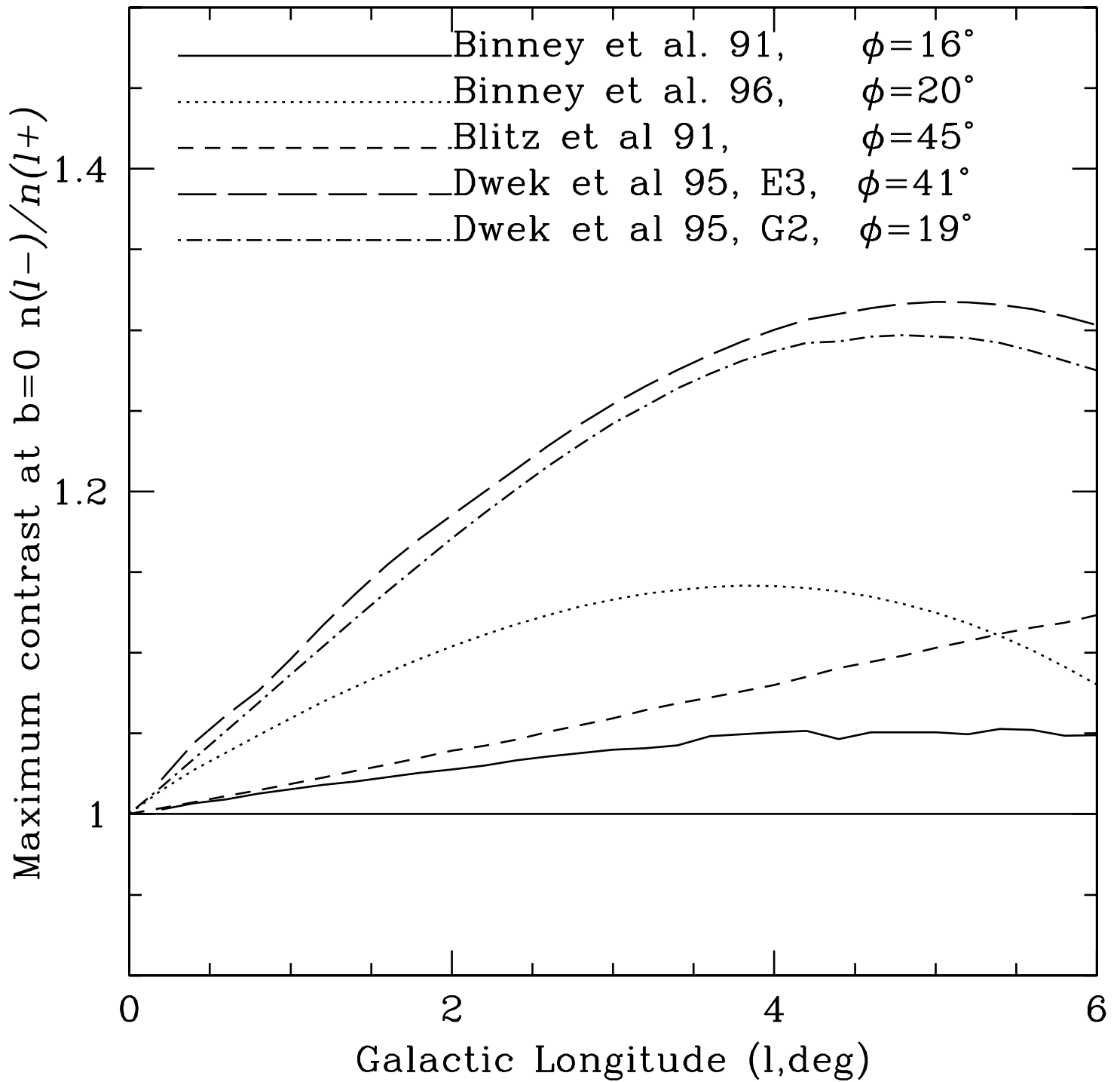


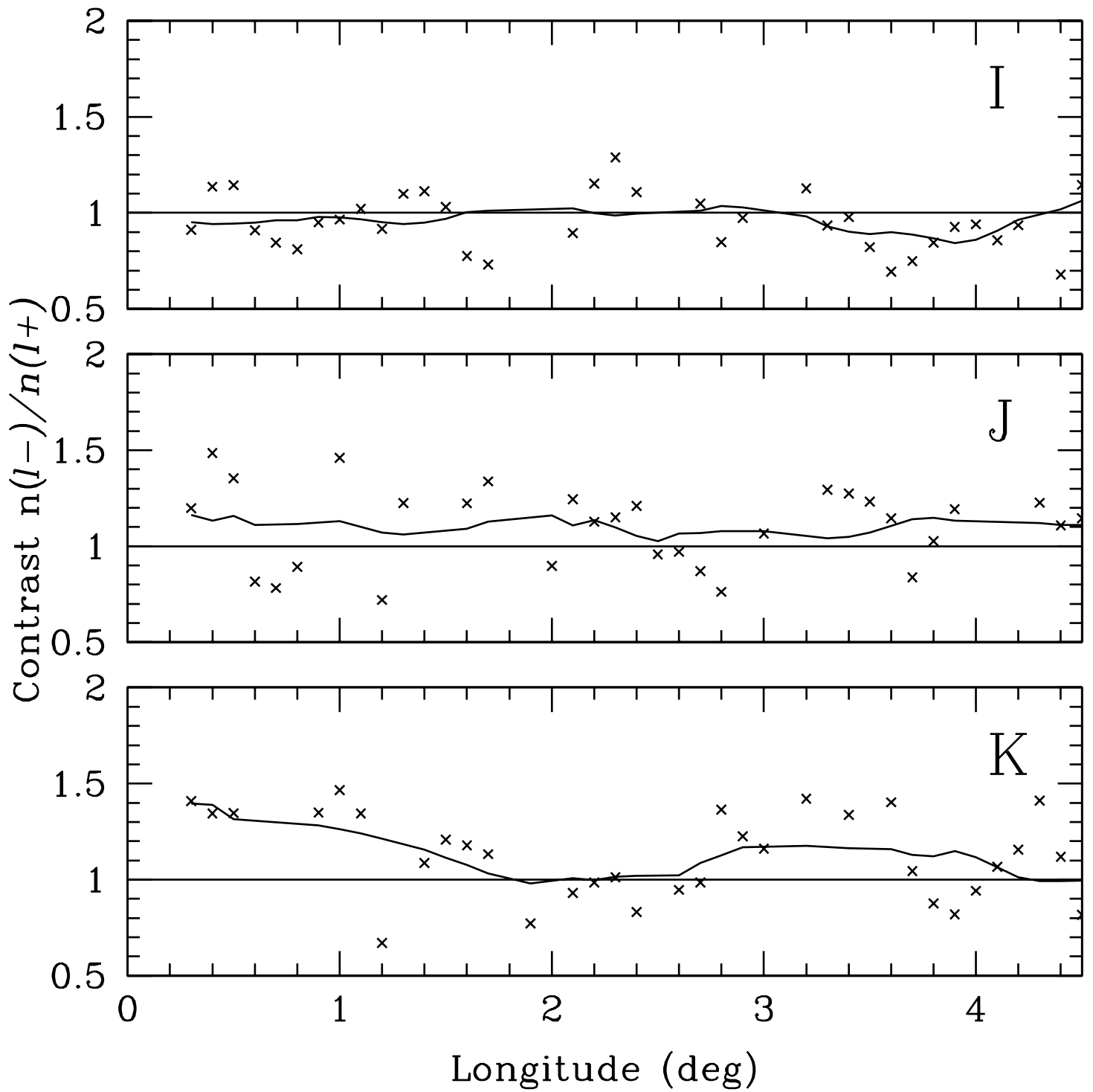
This figure "figure22.gif" is available in "gif" format from:

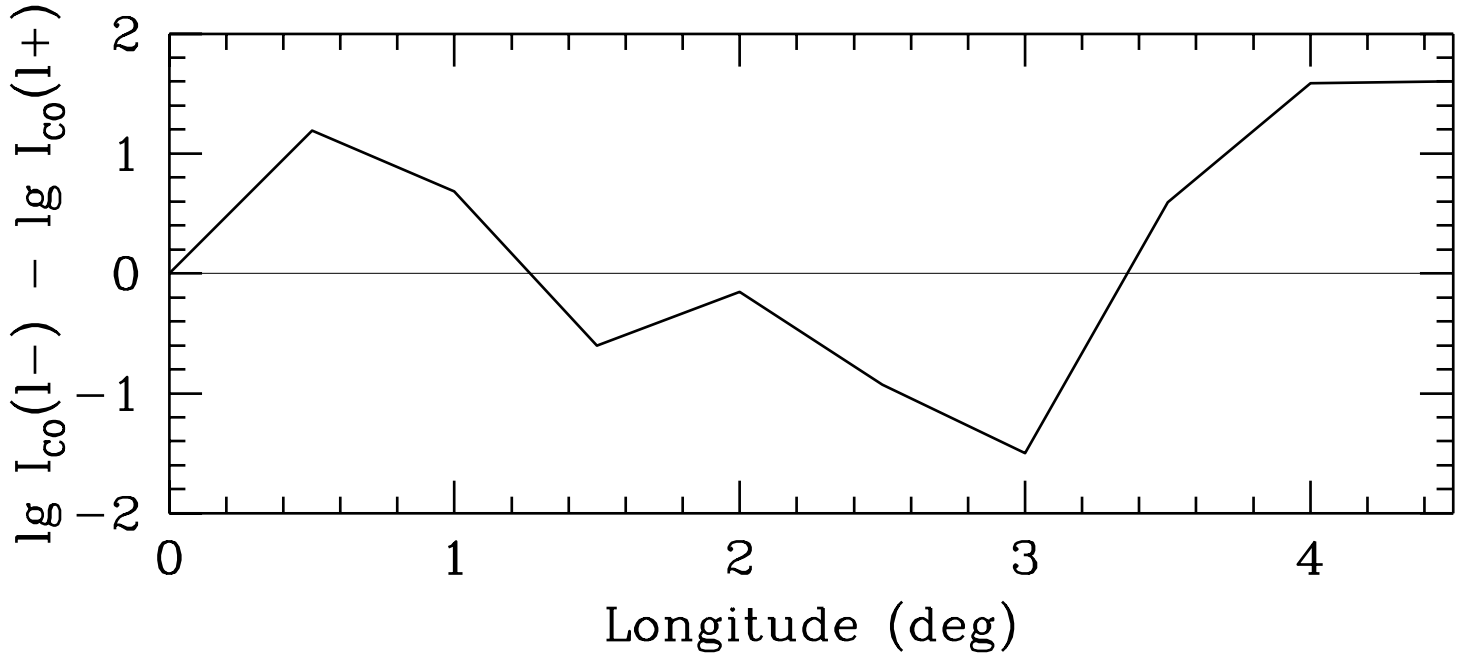
<http://arxiv.org/ps/astro-ph/9710317v1>

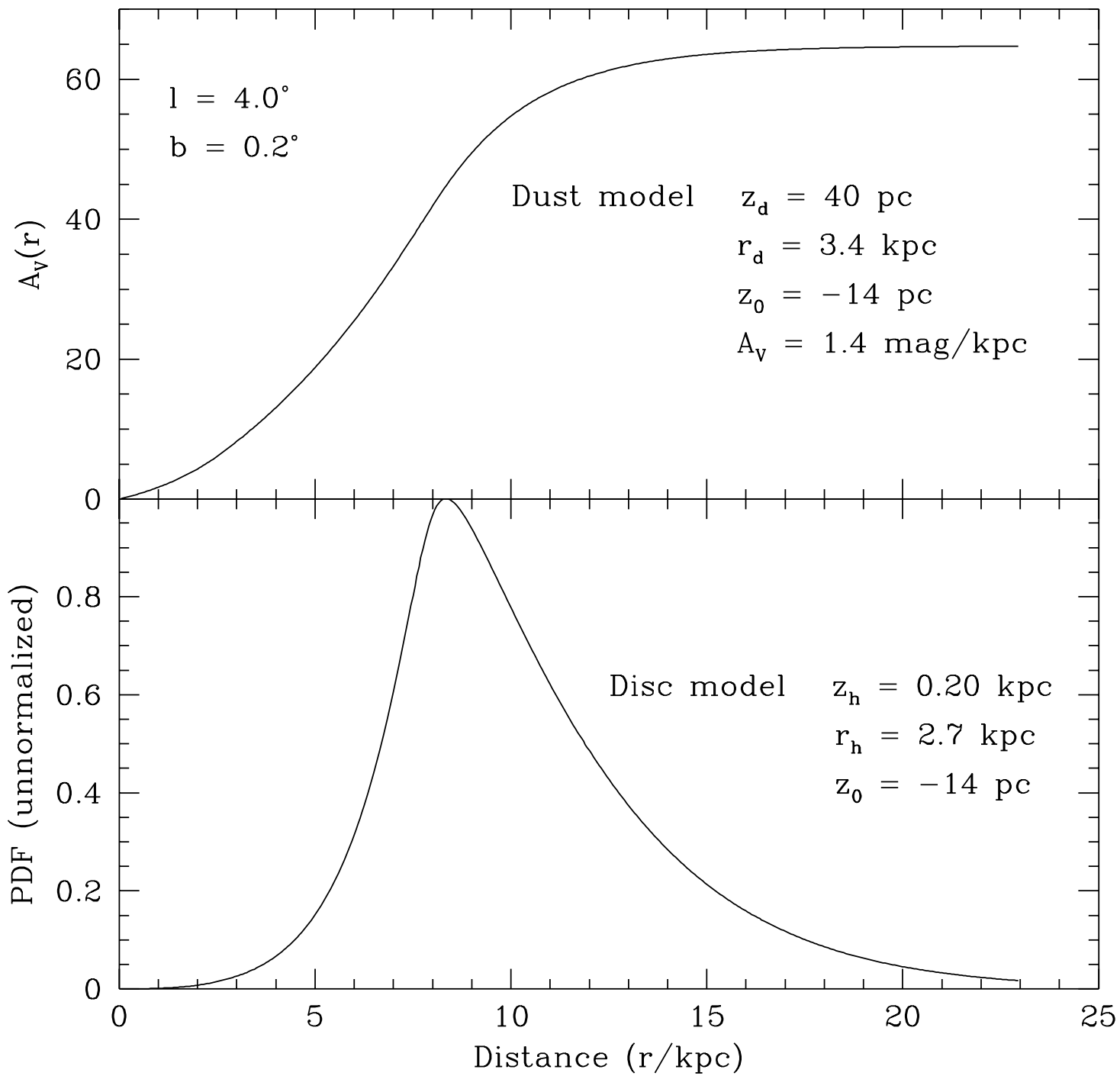
This figure "figure23.gif" is available in "gif" format from:

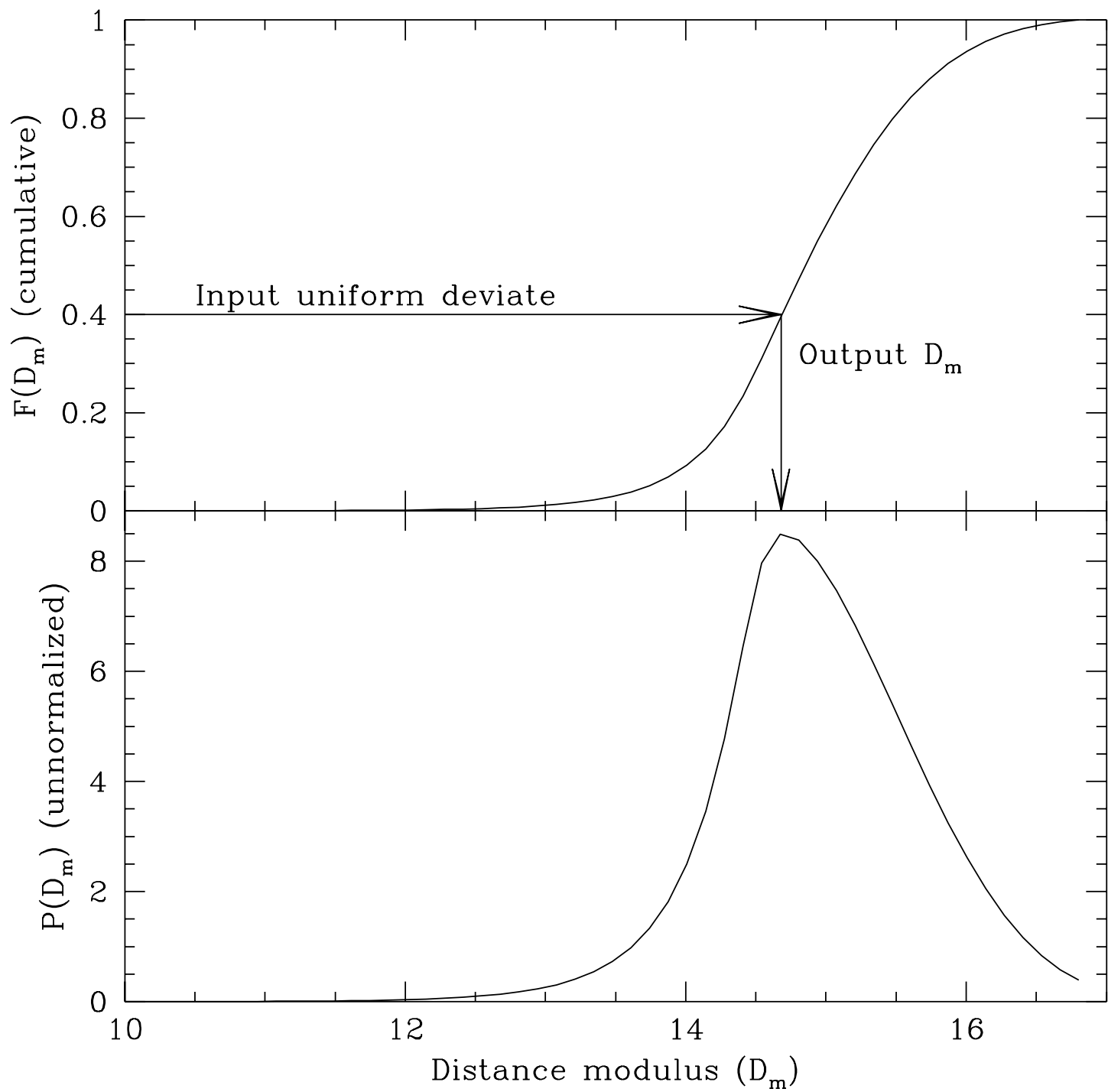
<http://arxiv.org/ps/astro-ph/9710317v1>

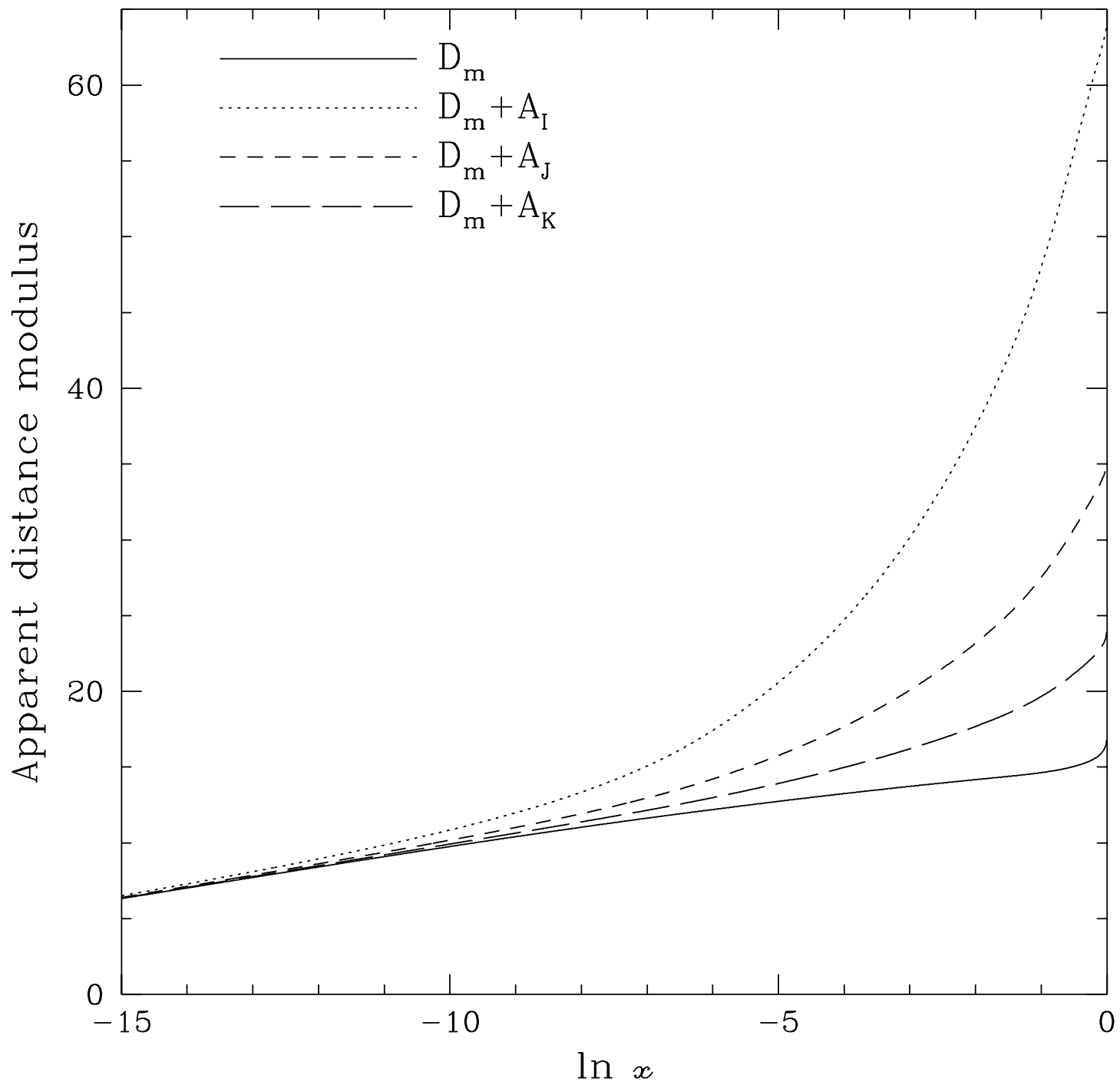


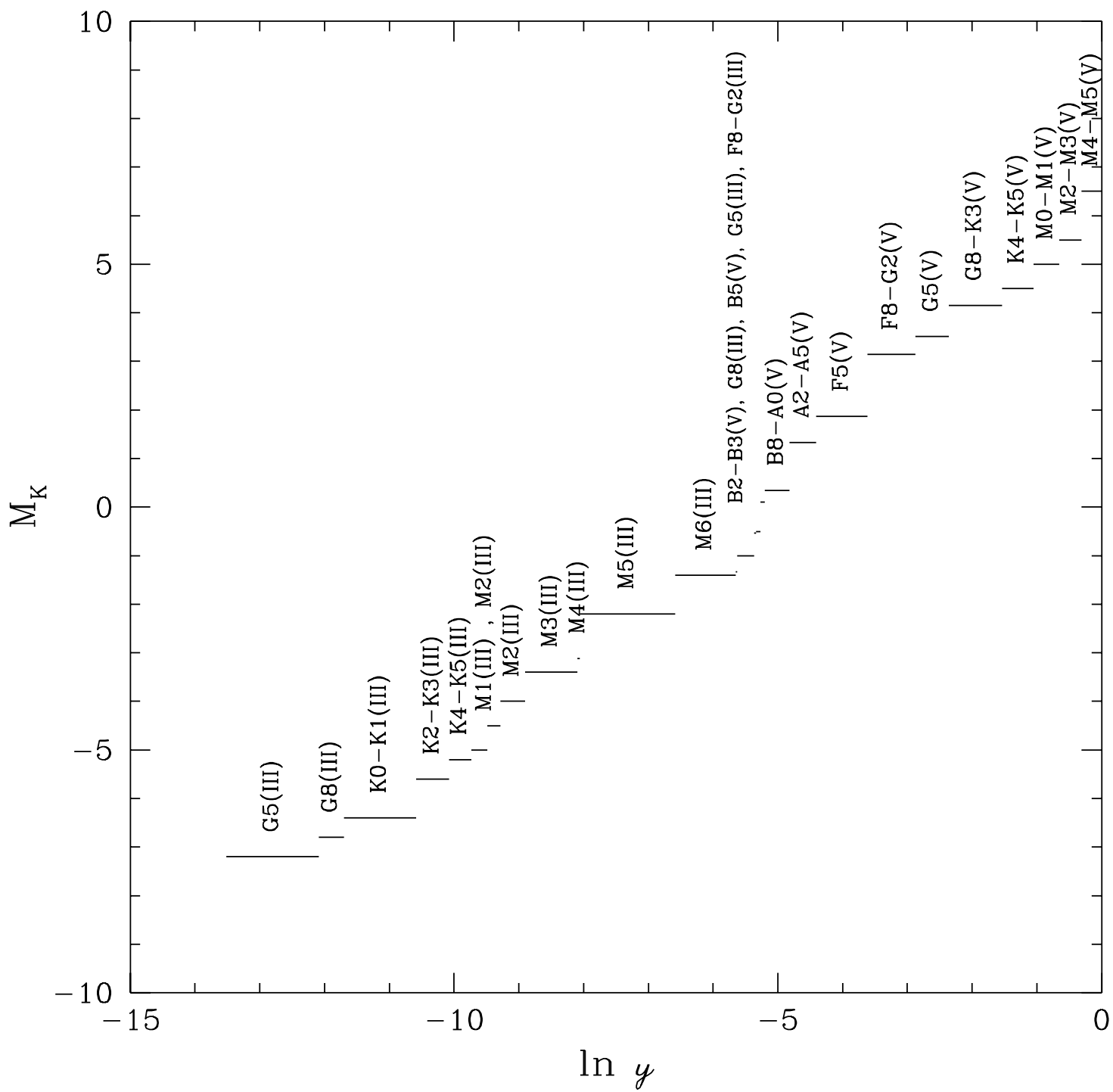


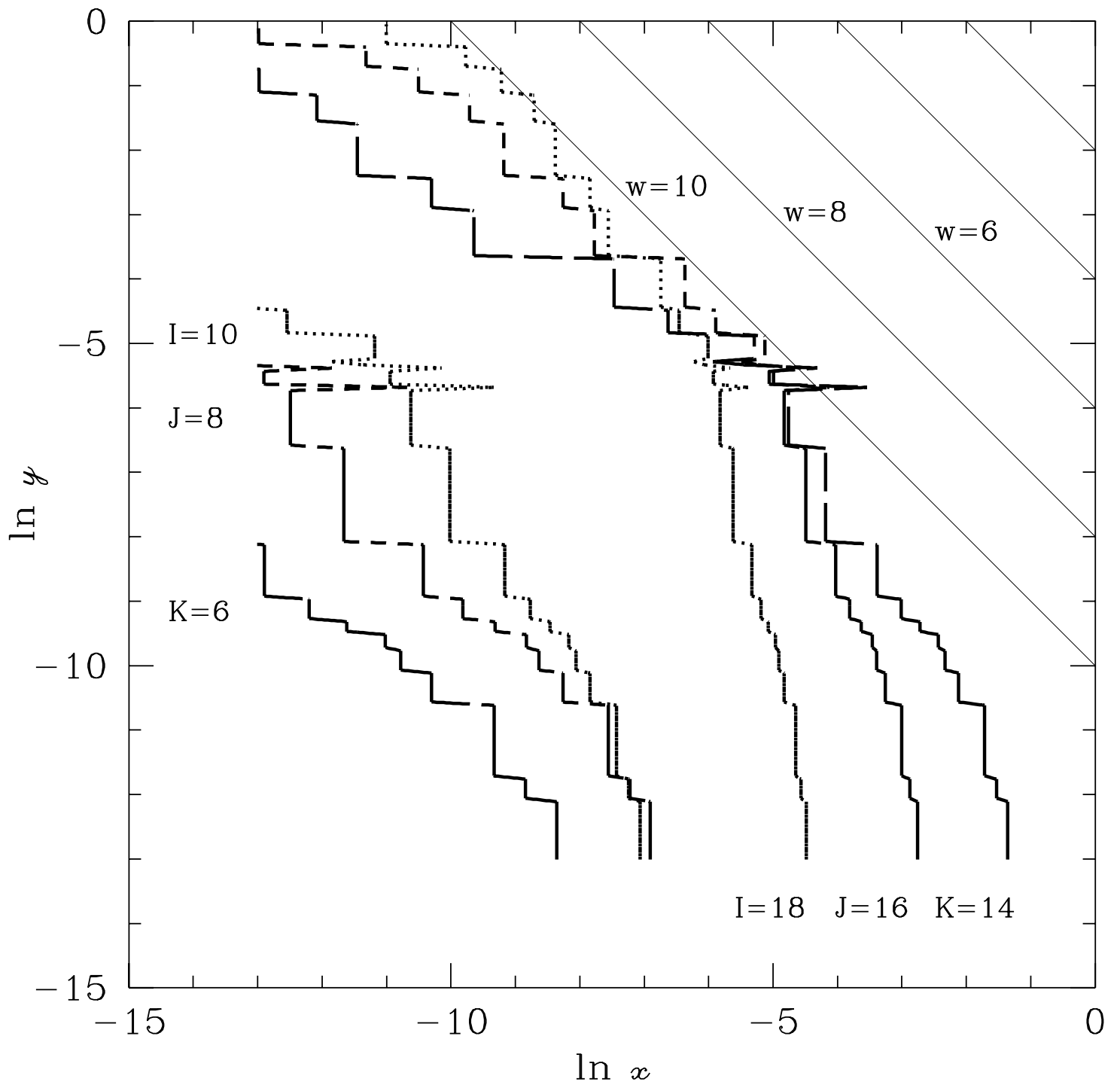


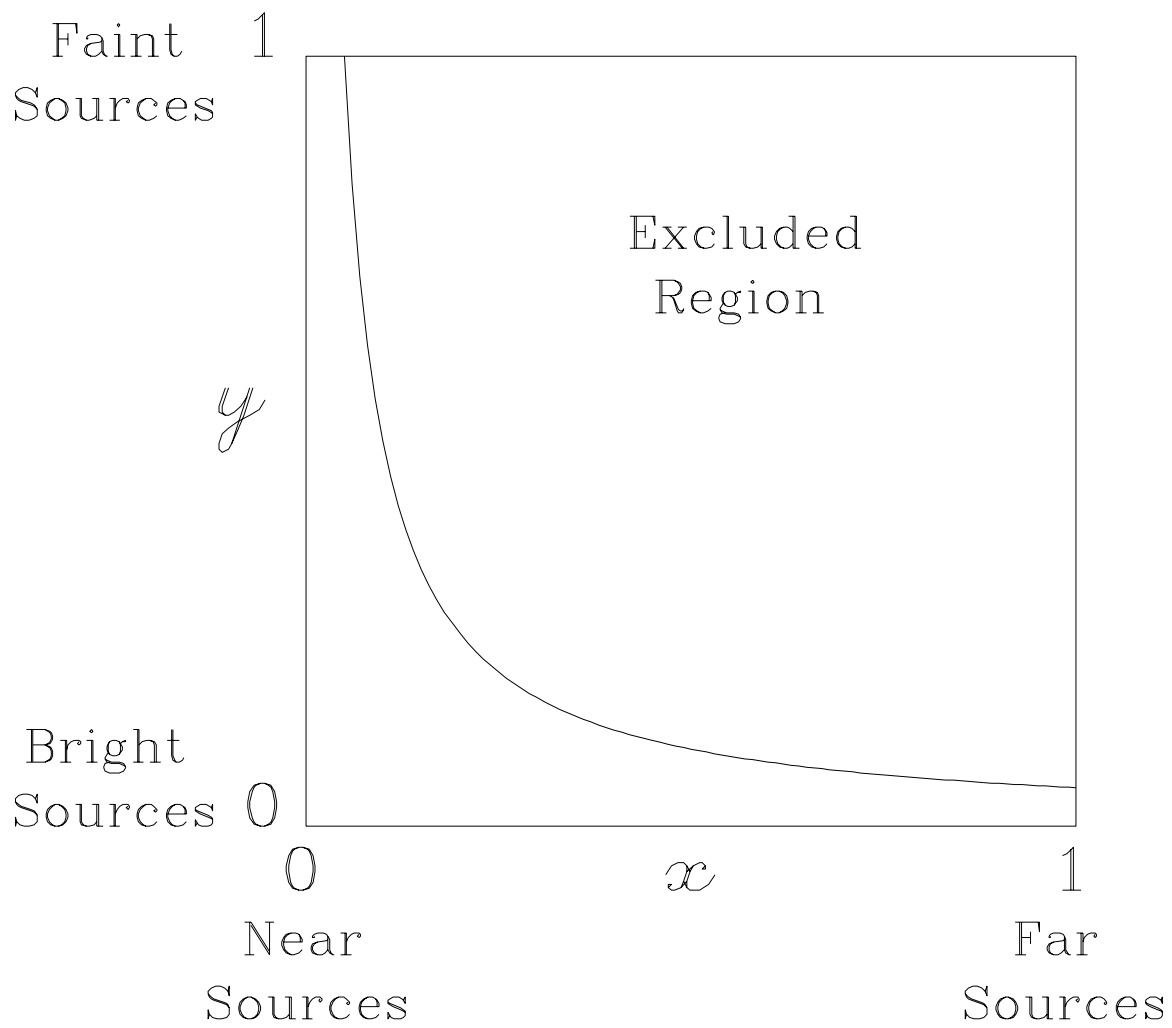












This figure "figure33.gif" is available in "gif" format from:

<http://arxiv.org/ps/astro-ph/9710317v1>